Seasonal and Interannual Variability of Areal Extent of the Gulf of Mexico Hypoxia from a Coupled Physical-Biogeochemical Model: A New Implication for Management Practice

Article · May 2019

DOI: 10.1029/2018JG004745

CITATIONS
0

READS
99

4 authors, including:

Yang Feng
South China Sea Institute of Oceanology Chinese Academy of Scicence
9 PUBLICATIONS **226** CITATIONS
SEE PROFILE

Huijie Xue
University of Maine
111 PUBLICATIONS **2,388** CITATIONS
SEE PROFILE

JGR Biogeosciences

RESEARCH ARTICLE
10.1029/2018JG004745

Key Points:
- Monthly hypoxia frequency is predominantly east-west, with seasonal maximum occurring in June, July, or August
- Satellite sea surface salinity, Chl *a*, and wind can be used with empirical relations to map spatiotemporally continuous bottom dissolved oxygen fields
- More nitrogen reduction will be needed to reduce hypoxic area to 5,000-km^2 target once the maximum hypoxic area could be known

Supporting Information:
- Supporting Information S1

Correspondence to:
Y. Feng,
yfeng1982@126.com

Citation:
Feng, Y., DiMarco, S. F., Balaguru, K., & Xue, H. (2019). Seasonal and interannual variability of areal extent of the Gulf of Mexico hypoxia from a coupled physical-biogeochemical model: A new implication for management practice. *Journal of Geophysical Research: Biogeosciences*, *124*. https://doi.org/10.1029/2018JG004745

Received 15 AUG 2018
Accepted 8 MAY 2019
Accepted article online 31 MAY 2019

Seasonal and Interannual Variability of Areal Extent of the Gulf of Mexico Hypoxia from a Coupled Physical-Biogeochemical Model: A New Implication for Management Practice

Yang Feng[1,2,3], Steven F. DiMarco[2], Karthik Balaguru[4], and Huijie Xue[1]

[1]State Key Laboratory of Tropical Oceanography, South China Sea Institute of Oceanology, Chinese Academy of Sciences, Guangzhou, China, [2]Department of Oceanography, Texas A&M University, College Station, TX, USA, [3]Institution of South China Sea Ecology and Environmental Engineering, Chinese Academy of Sciences, Guangzhou, China, [4]Marine Sciences Laboratory, Pacific Northwest National Laboratory, Sequim, WA, USA

Abstract The extent of hypoxia on the Louisiana shelf has been measured during July since 1985. The measured area was assumed to represent the seasonal maximum each year and was related to the Mississippi-Atchafalaya riverine May NO_{2+3} loading and May–June total nitrogen loading, for planning management strategies. In this study, we analyze 25 years of simulations from a coupled physical-biogeochemical model. An empirical orthogonal function analysis of the hypoxia frequency reveals that the dominant pattern is east-west, with the seasonal maximum occurring in June, July, or August. This indicates that the July hypoxic area may or may not always be the largest of the year. A simple linear regression model was constructed to examine the explained variance of hypoxia attributable to nutrients. Results reveal that the May NO_{2+3} (May–June total nitrogen) loading can explain 35% ± 7% (54% ± 7%) of the maximum cumulative hypoxic area in contrast to 22% ± 9% (48% ± 12%) of the July cumulative hypoxic area. Our results suggest that the current nitrogen loading reduction suggested by the Hypoxia Task Force 2013 is not sufficient to reduce the 5-year moving average Gulf's hypoxic zone to less than 5,000 km^2. A reduction of at least 66% (48%) of May NO_{2+3} (May–June total N) loading is needed when using July hypoxic area as the criterion, while a reduction of 77% (60%) of May NO_{2+3} (May–June total N) loading is needed when using maximum hypoxic area.

Plain Language Summary Shelf-wide surveys of hypoxia have been conducted in July since 1985 over the Texas-Louisiana shelf. The measured hypoxic area has been used as the metric for hypoxia severity. Management practices have been designed based on this metric to control the amount of nitrogen loading to the Mississippi River Basin. Our analysis of 25 years of model output reveals that the reported measured area may not always be the largest of the year. Therefore, using July hypoxic area will underestimate the reduction in nutrient loading required to achieve a 5,000-km^2 area required reduction in nitrogen.

1. Introduction

Oxygen depletion can cause detrimental ecological effects in coastal waters and is therefore a serious management concern, which has led to many scientific studies (Díaz & Rosenberg, 2008; Ekau et al., 2010; Osterman et al., 2009; Rabalais et al., 2014). In the Gulf of Mexico, water with oxygen concentration lower than 2 mg/L is considered hypoxic (Hofmann et al., 2011). The region of hypoxia in the Gulf of Mexico is believed to have increased since the midtwentieth century.

Traditionally, statistical analysis has linked the recurring hypoxia on the Louisiana shelf to the high winter and spring nutrient inputs from the Mississippi-Atchafalaya River. Riverine nutrients stimulate high rates of primary production (PP) in coastal waters; as the organic matter sinks below the pycnocline and decomposes, dissolved oxygen (DO) is depleted by microbial respiration (Greene et al., 2009; Rabalais et al., 2002, 2010; Rabalais, 2004; Turner & Rabalais, 1994; Turner et al., 2005). In addition, as winds are generally from the west and weak during summer, the freshwater introduced by the Mississippi-Atchafalaya River causes the shelf to be stratified, preventing the reoxygenation of the bottom water and thus maintaining the low oxygen conditions of bottom water (Cho et al., 1998; Cochrane & Kelly, 1986).

The Louisiana shelf-wide survey of hypoxia has been conducted once per year during July since 1985. The measured bottom DO concentration has been used to estimate the areal extent of hypoxia. Turner et al. (2006) explained the change in hypoxic area using linear regression models, with May NO_{2+3} loading as predictors. Scavia et al. (2003) reproduced the hypoxic area using a one-dimensional biophysical oxygen model, driven by the May–June total nitrogen loading. These two models are widely used to develop management strategies to control the size of the hypoxic area (Rabalais et al., 2002, 2007; U.S. Environmental Protection Agency, 2001, 2007, 2008, 2013).

The complexity and variability of physical processes in the coastal systems drive the interannual variation of the Louisiana hypoxic area. Feng et al. (2014) used a coupled three-dimensional physical-biogeochemical model and found that the hypoxic area in the year 2009 reached its maximum in June and decreased afterward. Turner et al. (2006) noticed that strong storms 3 weeks before the measurements in the year 2003 greatly reduced the measured hypoxic area. These interannual variations indicate that the measured hypoxic area in July may or may not always be the largest area of the year. The interannual variability may complicate the "nutrient-hypoxia" relation, which could reduce the success of nutrient regulation practices in managing Gulf hypoxia.

The objectives of this study are to (1) explore mechanisms controlling the timing of maximum hypoxia, (2) investigate differences in the relationships between nutrients and July hypoxia and between nutrients and maximum hypoxia, and (3) discuss how this impacts management practices for Gulf of Mexico hypoxia. Our study is based on a space and time resolving, three-dimensional, coupled physical-biogeochemical model. Section 2 and Appendices A and B give a full description of the model and in situ observations used to validate the model; section 3 contains the results. We discuss the model validation, the spatiotemporal variability of hypoxia, and the associated controlling mechanisms. We also examine the relationship between nutrients and hypoxia when taking the July and maximum criteria and discuss how management practices perform differently. Section 4 discusses the limitations of the current model and implications of the results. Section 5 summarizes result and future works.

2. Data and Methods

2.1. Model Description

The hydrodynamic component of the coupled model is the state-of-the-art Regional Ocean Modeling System (ROMS; Shchepetkin & McWilliams, 2005). The model configuration is detailed in Hetland and DiMarco (2008, 2012). The model domain spans the region 94.7–87.7°W, 27.4–30.4°N, covering the shelf region where the oxygen concentration has been measured routinely since 1985. A full description of the hydrodynamic model is given in Appendix A. The skill of the hydrodynamic model for temperature, salinity, and current velocity was assessed by Hetland and DiMarco (2012), who demonstrated that the model performs fairly well in simulating the shelf circulation and stratification as well as their seasonal variation.

The biological component of the coupled model is a modified version of the nutrient-phytoplankton-zooplankton-detritus marine ecosystem model of Fasham et al. (1990), which represents a simplified nitrogen cycle with seven state variables: nitrate (NO_3), ammonium (NH_4), phytoplankton (P), zooplankton (Z), small (D_S) and large detritus (D_L), and chlorophyll (CHL; Fennel et al., 2006, 2008). Application of the nitrogen cycle model to the northern Gulf of Mexico was described and validated in Fennel et al. (2011), and DO was added to the model as an additional state variable as described in Feng et al. (2012) and Fennel et al. (2013). The initial values for biological and nutrient components were uniform over the model domain. The oxygen concentrations were initialized with the saturation values calculated from the associated temperature and salinity profiles. The model was run from 1980 to 2009 with the first 5 years removed from the analysis to account for spin up time. Equations and parameters used in the biogeochemical model are described in Appendix B.

2.2. Observations

A long-term time series from fixed moorings (stations C6A, C6B, C6C/CSI-6, and CSI-9) and a series of monthly to bimonthly cruises along two fixed cross-shore transects (C and F) for 1985–2009 are used to evaluate the model's performance in capturing the seasonal variation of DO concentration from surface to bottom (Table 1 and Figure 1). The observations are part of an ongoing program at the Louisiana

Table 1
Available Louisiana Universities Marine Consortium Hypoxia Data for Stationary Moorings C6X and Cross-Shore Transects (C and F) From National Oceanography Data Center for 1985–2009

Year	Moorings	Transects
1985	N/A	C Jun–Dec F Jul
1986	N/A	C Jan, Mar–Nov F Jul
1987	N/A	C/F Jul
1990	C6 Apr–Jun, Aug–Nov C6A Mar–Jun, Aug–Nov	C Apr–Nov F Jul
1991	C6 Feb–Jun, Aug–Oct, Dec C6A Feb–Jun C6B Feb–Dec	C Feb–Dec F Jul
1992	C6 Mar–Jun, Aug, Sep C6B Mar–Oct	C Mar–Oct F Jul
1993	N/A	C/F Jul
1998	C6B Jan–Sep, Nov–Dec	C/F Jul
1999	C6B Jan, Mar–Dec	C Jul, Aug F Jul
2000	N/A	C/F Jul
2001	C6 Jan, Mar, Apr, Oct C6B Jan, Mar, Apr, Jul, Oct–Dec	C Jan, Mar, Apr, Jul, Oct–Dec F Jan, Mar, Jul, Nov, Dec
2002	C6 Jan, Feb, May, Jun, Aug–Oct C6B Jan–Oct	C Jan–Oct F Feb, Apr, Jun–Aug, Oct
2003	C6 Apr, Jun, Sep–Dec C6B Jan, Feb, Apr, Jun, Jul, Sep–Dec	C Jan, Feb, Apr, Jun, Jul, Sep–Dec F Jan, Feb, Apr, Jun, Jul, Sep–Dec
2004	C6 Jan–Jun, Aug, Oct, Nov C6B Jan C6C Feb–Aug, Oct, Nov	C Jan–Aug, Oct, Nov F Feb, Apr, Jun, Jul, Nov
2005	C6 Jan, Feb, Jul, Nov, Dec C6C Jan, Feb, Jul, Nov, Dec	C Jan–Dec F Feb, Jun–Aug, Oct
2006	C6 Jan–Aug, Nov C6B Mar, Jun–Aug, Nov C6C Jan–Aug, Nov	C Jan–Aug, Nov F Feb, Apr, Jun–Aug
2007	C6 Jan, Feb C6B Jan, Mar, May–Aug, Oct, Nov C6C Jan–Mar, May–Dec	C Jan–Mar, May–Dec F Jan, Mar, May, Jul
2008	C6B Apr–Aug C6C Jan–Aug, Oct, Nov	C Jan–Aug, Oct, Nov F Feb, Apr, Jun, Jul, Nov
2009	C6C Jan, Feb, Mar, Apr, May, Jul	C Jan, Feb, Mar, Apr, May, Jun, Jul, Aug, Sep, Oct F Jan, Mar, Jul, Aug, Oct

Universities Marine Consortium. The data were archived by the National Center for Environmental Information (https://www.nodc.noaa.gov/access/index.html). Measurements from moorings document the vertical structure and monthly DO concentrations at fixed sites near the mouth of the Mississippi River. An interdisciplinary mooring array has been deployed in about 20-m water depth south of Terrebonne Bay since 1989. The temporal coverage from these moorings varies from year to year. Since most stations (C6A, C6B, and C6C/CSI-6) are too close to each other to be resolved by the numerical model, they are considered as one station (C6X) for model/observation comparisons. Two cross-shore transects have been sampled monthly or bimonthly for oxygen distribution near the Mississippi (C) and Atchafalaya (F) River outflow regions. Transect C has been conducted monthly since 1990. Transect F has been conducted bimonthly since 2000. The observations are separated into summer (June, July, and August) and nonsummer months (September to May). In addition, as mentioned in the introduction, hypoxia shelf-wide surveys have been conducted once per year during July since 1985. Table 2 lists the estimated hypoxic area for the 25 years in our study. There was no measurement in 1989.

2.3. Statistical Analysis

Empirical orthogonal function (EOF) analysis simplifies a spatiotemporal data set by transforming it into spatial patterns of variability and temporal projections of these patterns. The spatial patterns are the EOFs and can be thought of as basis functions in terms of variance. The associated temporal projections are the principal components (PCs) and are the temporal coefficients of the EOF patterns (Emery & Thomson, 2001).

We analyze the 25-year (1985–2009) simulated bottom DO field to examine typical spatial and temporal patterns of hypoxia. Because the oxygen concentration changes rapidly, results at monthly time intervals provide a more statistically robust pattern than the instantaneous DO concentration. We count the number of days that are hypoxic in each month and divide the total number of days in that month for each model grid, yielding a frequency of hypoxia occurrence. Locations with "0" indicate no hypoxia during a month, and "1" indicates persistent hypoxia. Prior to the EOF calculation, the mean field, which represents the average annual monthly frequency had been averaged over the whole studied period and subtracted. The threshold (3 mg/L) for simulated DO, different from that adopted for the observed DO, has been used in some other modeling of hypoxia (Liu et al., 2010; Scavia et al., 2003). We provide a full discussion of the bottom DO threshold in section 4.

We use a simple linear regression model ($y = \beta_1 x + \beta_0$) to investigate the difference between the nutrient-July hypoxia relationship and the nutrient-largest hypoxia relationship. Simple linear regression concerns two-dimensional sample points with one independent variable and one dependent variable and finds a linear function predicting the dependent variable values as a function of the independent variable. The regression analysis was performed using MATLAB, which uses standard least squares methods to estimate the slope coefficient β_1, a measure of the sensitivity of the dependent variable to the independent variable, as well as the coefficient of determination r^2, which assesses how well a model explains and predicts future outcomes. The May NO_{2+3} and May–June total nitrogen loading are used as independent variables x here. They are the most widely used nutrient metrices both for hypoxia prediction and management practices (Scavia et al., 2003; Turner et al., 2006). The dependent variables y are the hypoxia data sets, including (1) the monthly cumulative hypoxic area, which is calculated by integrating

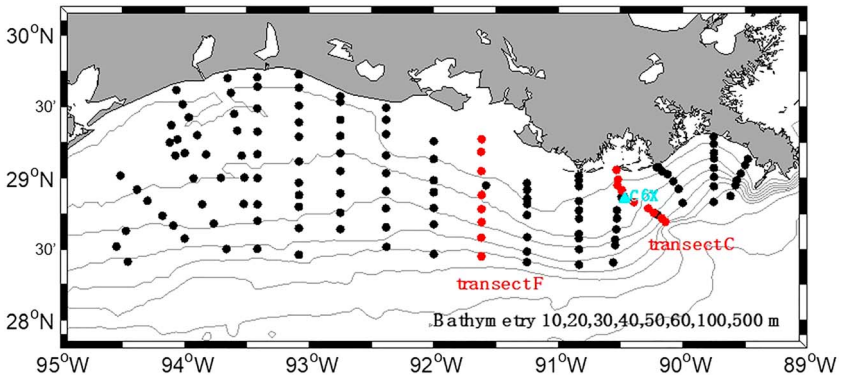

Figure 1. The sites for sampling programs. Actual locations may vary from year to year. The fixed moorings are close to each other and shown as C6X (blue triangle). Red dots are the transects C and F. The stations on transect C from nearshore to offshore are C1, C3, C5, C6, C7, C8, C9, C10, and C11. The stations on transect F from nearshore to offshore are F0, F1, F2, F3, F4, F5, F6, and F7.

the model grid areas where bottom DO concentration is less than 3 mg/L within the 100-m isobath in each month and (2) the along-shelf hypoxia component, which is the hypoxia frequency indicator extracted from the first PC time series. We use two sets of data to calculate these hypoxia metrics: model output from July (because this is the month when the hypoxia shelf-wide survey is conducted) and from the month that exhibits the largest hypoxia each year. We notice that the ability of nutrients to explain the hypoxic area reported in the literature depends on the length of the study period; for example, the May NO_{2+3} explains 50% of area variability for the study period ending in 2004 (Turner et al., 2006), 42% for period ending in 2007 (Greene et al., 2009), and only 33% for the period ending in 2010 (Feng et al., 2012). To address this issue, we ran the regression for periods ending from 1993 through 2009 (i.e., analysis periods ranging from 9 to 25 years) to ensure the results are robust.

Cross correlation is a measure of similarity of two time series as a function of the displacement of one relative to the other. The cross correlations were calculated by computing the correlation coefficients between the two above-mentioned hypoxia data sets and different physical and biogeochemical data sets, which are lagged between 1 and 6 months. The biogeochemical metrices are (1) the combined Mississippi-Atchafalaya River flow, (2) the dissolved inorganic nitrogen (DIN NO_2 NO_3 NH_4) concentration of the Mississippi River, (3) the DIN concentration of the Atchafalaya River, (4) the particulate and dissolved organic nitrogen (PON + DON) concentration of the Mississippi River, (5) the PON + DON concentration of the Atchafalaya River, (6) Atchafalaya and Mississippi DIN loading (DIN concentration times River flow), (7) Atchafalaya and Mississippi PON loading (PON concentration times River flow), (8) Atchafalaya and Mississippi total N loading (DIN loading plus PON loading), (9) spatially averaged wind speed, and (10) spatially averaged wind direction. The physical (two-dimensional) data sets used for the cross correlations include (1) the North America Regional Reanalysis wind speed, (2) the North America Regional Reanalysis wind direction, (3) the sea surface salinity derived from the model, and (4) the surface chlorophyll derived from the model.

Table 2
Estimated Hypoxic Area From the July Cruises

Year	Hypoxic area (km^2)	Year	Hypoxic area (km^2)
1985	9,774	1998	12,480
1986	9,432	1999	20,000
1987	6,688	2000	4,400
1988	40	2001	20,720
1989	—	2002	22,000
1990	9,260	2003	8,560
1991	11,920	2004	15,040
1992	10,804	2005	11,840
1993	17,600	2006	17,280
1994	16,600	2007	20,500
1995	18,200	2008	20,720
1996	17,920	2009	8,000
1997	15,840		

Lastly, a note regarding DO units. The most commonly used units are milligrams per liter (mg/L), parts per million (ppm), milliliters per liter (mg/L), and micromolars (μM). Hypoxia in the Gulf of Mexico is defined as DO concentrations less than 2 mg/L, which is the equivalent of 2 ppm, 1.4 ml/L, or 62 μM. We use both mg/L (commonly used in observations) and μM (commonly used in models) throughout this article.

3. Results

3.1. Model Validation

3.1.1. Comparisons With Long-Term Observations at C6X

The model captures the general vertical structure and the seasonal variation of the observed DO concentration for the time series station C6X

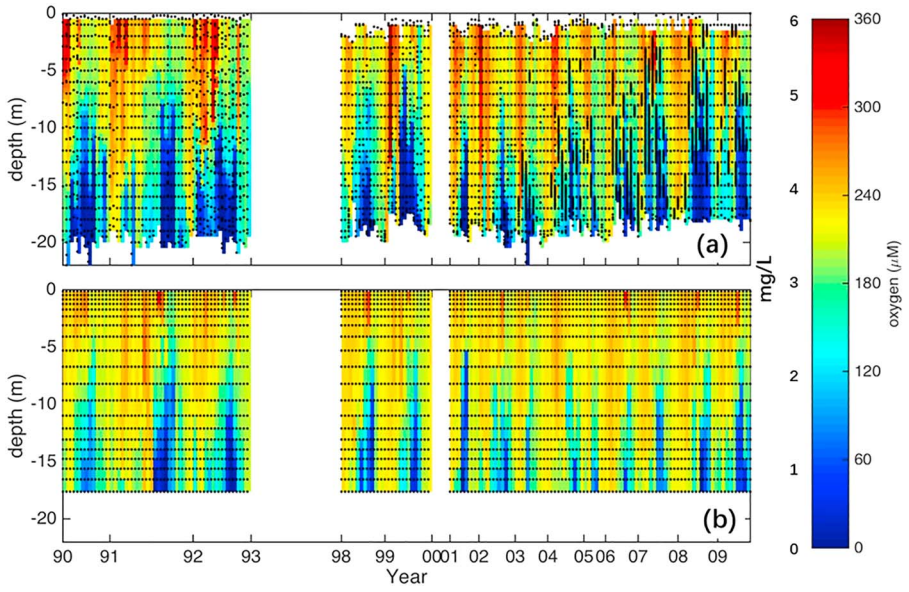

Figure 2. Oxygen concentrations at the fixed mooring C6X. (a) Observations, black dots are the sample locations. (b) Simulation, black dots denote the model vertical grid.

(Figure 2). In the layer above 5 m, the observed (modeled) mean DO concentration is 264 ± 13 μM (264 ± 38 μM) before June, 210 ± 11 μM (208 ± 25 μM) from June to August, and 215 ± 5 μM (214 ± 28 μM) after August. In contrast to the surface measurements, the modeled bottom DO concentrations are higher than those observed. Below 15-m depth, the observed (modeled) DO concentration is 158 ± 12 μM (187 ± 8 μM) before June, 45 ± 18 μM (89 ± 10 μM) from June to August, and 157 ± 13 μM (188 ± 7 μM) after August. Below 18-m depth (the last model grid cell), the observed (modeled) DO concentration is 152 ± 6 μM (187 ± 31 μM) before June, 32 ± 4 μM (64 ± 6 μM) from June to August, and 149 ± 11 μM 15 (187 ± 37 μM) after August. Two simple skill metrics, bias and correlation coefficient (r), are used here for measuring the discrepancies and covariance between the model and observations, respectively. We interpolate observations to the model grid for ease of comparison. For the bottommost layer in the model, the coefficient of determination (r^2) is about 0.52 and the bias is about 1 mg/L (Table 3). The overestimation of bottom oxygen will be discussed in section 4.

3.1.2. Model-Observation Comparisons for Transects C and F

For both transects C and F (Figures 3 and 4), we average all available observations at each model grid depth every month and plot them as colored dots. The background color is the multiple-year model average. The more the dots blend with the background color, the more model and observations agree. Here we found that at the vertical transect C, the model is very consistent with observations during winter. The DO concentration stays high from surface to the bottom with DO concentration around 240 μM. The vertical gradient of DO concentration strengthens in June, July, and August. However, the simulated bottom DO concentration overestimates the observed bottom DO for inshore stations C1–C9 but underestimates it for offshore stations C10 and C11. The DO concentration in the bottommost grid cell is about 149 (70), 141 (52), and 146 (54) μM in the model (observations) in June, July, and August, respectively.

Table 3
Model Performance for Bottom Dissolved Oxygen Concentration at C6X, Transect C, Transect F, and Estimated Hypoxic Area

DO concentration/Estimated hypoxic area	Bias	r
C6X	1 mg/L (32 μM)	0.72
Transect C	0.9 mg/L (28 μM)	0.66
Transect F	0.6 mg/L (18 μM)	0.68
Hypoxic area using 2 mg/L	5,494 km^2	0.56
Hypoxic area using 3 mg/L	−1,100 km^2	0.75

The model agrees better with observations on transect F than transect C. The DO concentrations in the bottommost grid cell is about 146 (149), 129 (104), and 135 (93) μM in June, July, and August in the model (observations), respectively. Higher values of the DO concentration near the bottom diffuse upward more in August in the observations.

The model reproduces the observed DO seasonal variation and has strong vertical gradients. However, it smooths the oxygen fields relative to the observations and overestimates the bottom DO concentrations. We also quantify the model performance. The mean r^2 is 0.44 (0.46) mg/L, and the bias is 0.9 (0.6) mg/L for transect C (transect F; Table 3).

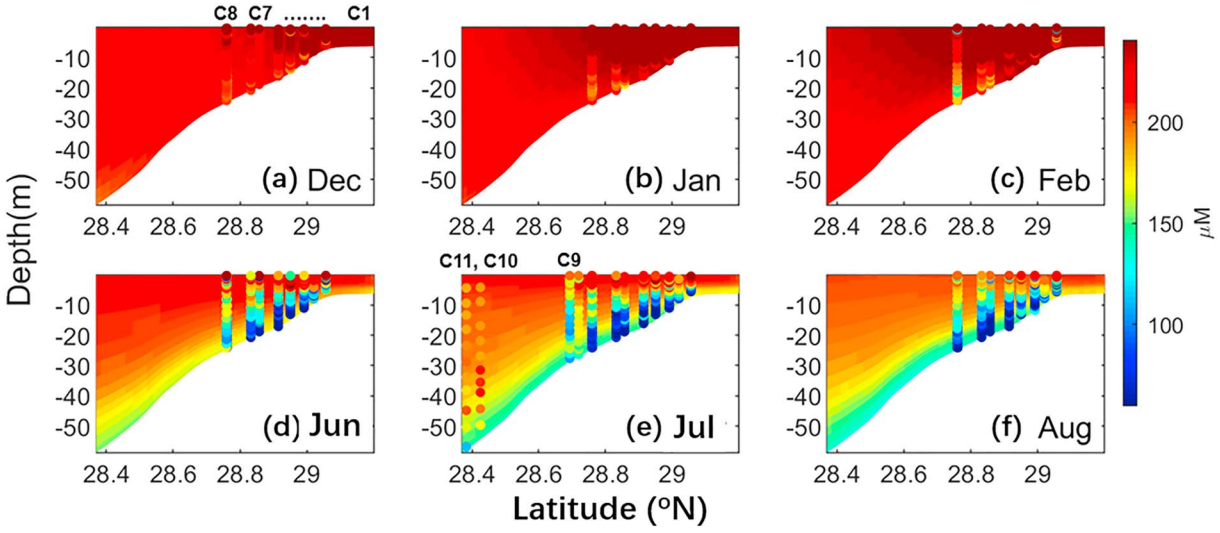

Figure 3. Observed (dots) and simulated (shading) dissolved oxygen concentrations along transect C during winter months (a) December, (b) January, and (c) February and summer months (d) June, (e) July, and (f) August.

3.1.3. Model-Observation Comparisons of the Hypoxic Area

The above comparisons of time series from station C6X and transects C and F show that the DO concentration fields from our model have a strong vertical gradient and seasonal cycle. However, the model overestimates the bottom DO concentration.

We calculate the total hypoxic area during each cruise period (e.g., 16–20 July 1991) by summing the area of all grid cells that have oxygen concentration below 2 and 3 mg/L. Then we compare the model-derived area with the area derived from the annual shelf-wide survey in Table 2 and Figure 5. The results show that they are highly correlated ($r^2 = 0.60$) with a negative bias of –4,745 km^2 when the 2-mg/L limit is used. Better correlation ($r^2 = 0.66$) and lower bias (1,431 km^2) are obtained when the 3-mg/L limit is used.

3.2. Variability of Hypoxia on the Louisiana Shelf

The monthly mean hypoxia frequency map shows that hypoxia occurs in areas <100-m depth east of Sabine Lake with a monthly frequency of 1% (Figure 6). Hypoxia is more frequent (≥10%) for bottom depths of 10–

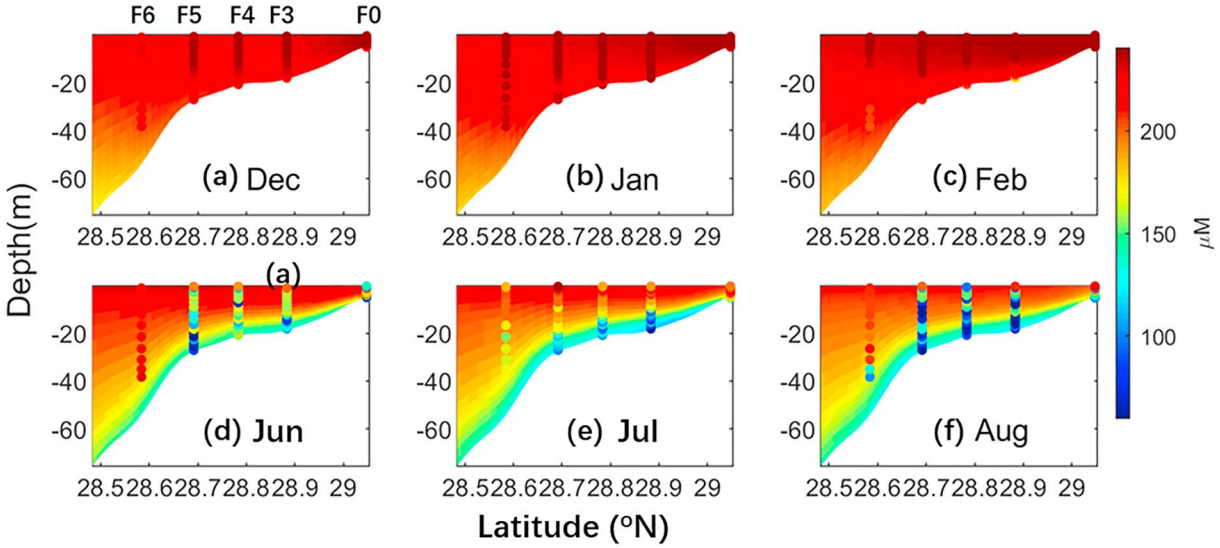

Figure 4. As in Figure 3 but for transect F.

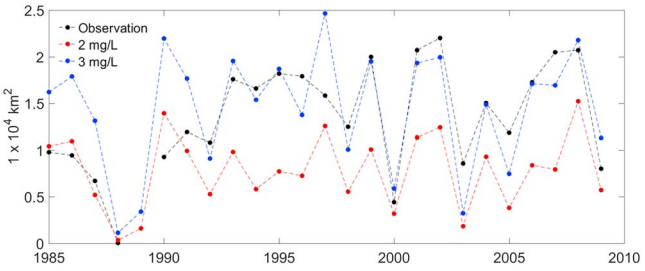

Figure 5. The observed and simulated hypoxic area at 2 and 3 mg/L during July cruises.

60 m east of Atchafalaya Bay. In the Louisiana Bight, the hypoxia frequency is greater than 20%. It is highest (≥50%) near the mouths of the Mississippi and Atchafalaya rivers.

An EOF analysis highlights the spatial and temporal aspects of the variability of hypoxia frequency (Figure 7). The first two modes explain 62% and 8.1% of the variance. The variance associated with the third mode is only 4.9% (not shown). The first two modes both have strong seasonal cycles that are evident in the monthly climatology of the PC values (Figure 7a).

The spatial pattern of the first EOF mode represents east-west variations (Figure 7c). West of Calcasieu Lake (about 93°W), the hypoxia signal is greatly diminished. It increases gradually eastward toward the Mississippi River Bird's-Foot Delta. The annual cycle shows that its contributions are positive from late spring to early fall (May–September) and peak in midsummer (July–August, Figure 7a). Thus, hypoxia intensifies from May through September and is largest in July–August. The spatial structure of the second (Figure 7d) EOF mode has a strong cross-shore pattern. The pattern reverses sign near the 10-m isobath. The PC time series documents the development of hypoxia. From April to July, hypoxia is predominantly confined to two distinct nearshore regions, beneath the Mississippi and Atchafalaya River plumes. From August to November, the two hypoxic regions move offshore and merge into one large region, located on the central and eastern part of the Louisiana shelf in waters shallower than 60 m.

The first PC time series also indicates strong interannual variability in addition to the seasonality (Figure 7b). The month when the first PC reaches its maximum varies with year, as does the magnitude. In most of the years studied the maximum is in July or August, with about equal numbers for each month. The exceptions are 1994 and 2009 when the maximum occurs in June.

3.3. Wind Control of the Onset of Hypoxia

The month in which the PC time series reaches its maximum during the summer is associated with the wind speed and direction (Feng et al., 2014; Yu, Fennel, & Laurent, 2015). To show the response of bottom DO concentration to different wind scenarios, we consider three different years: a typical wind year of 2002, the hurricane year of 2003, and the upwelling favorable wind year of 2009 (Figures 8a–8c). We plot the May–September bottom DO concentration along with several physical and biological variables, including the wind vector, wind speed, difference in surface and bottom salinity, difference in surface and bottom density, and the chlorophyll concentrations at station C6X (Figure 8).

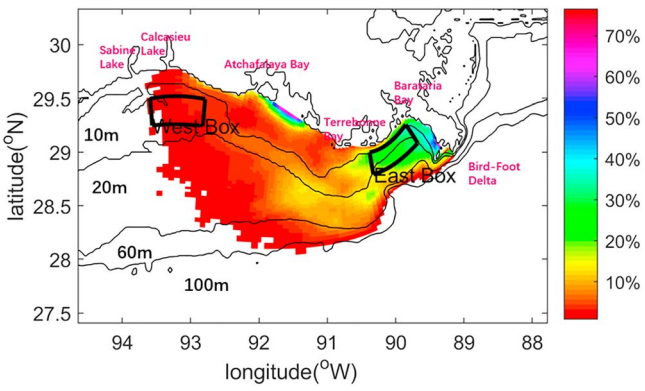

Figure 6. Mean monthly hypoxia frequency. The monthly frequency of hypoxia is calculated at each model grid cell by counting the number of days when the dissolved oxygen concentration was less than 3 mg/L. The model simulation was for the period 1985–2009 (300 months). The locations of the east and west boxes for oxygen mass budget analysis in Figure 9 are shown.

First, we found that the surface and bottom salinity and density differences are consistent, showing that the pycnocline on the Louisiana shelf is mainly generated by the Mississippi-Atchafalaya riverine freshwater input. Louisiana hypoxia is frequently observed within the 20- to 60-m depth range. The whole water column is heated throughout; hence, the temperature gradient contributes less to the strength of the pycnocline. Although the temperature does not contribute to the stratification, the annual cycle of temperature affects the annual cycle of bottom DO concentration. As the temperature increases during summer, the oxygen solubility decreases, causing the bottom water to have a higher tendency to develop hypoxia.

Second, we found there is a high surface chlorophyll concentration prior to the low bottom DO concentration. This reflects the response of bottom DO concentration to riverine nutrients because the high surface chlorophyll indicates the presence of strong PP, which is driven by high riverine DIN stimulating phytoplankton growth. As a result, a large amount of organic matter forms and accumulates over the eastern central Louisiana shelf, increasing the potential for hypoxia to occur over the Louisiana shelf.

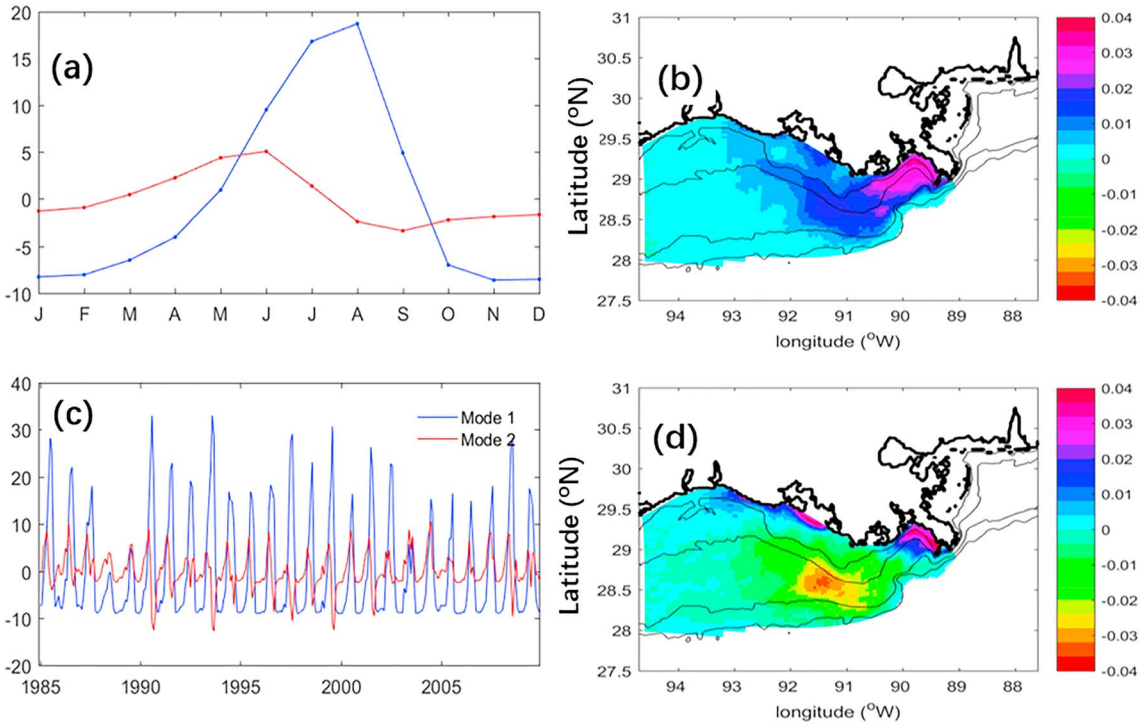

Figure 7. The first and second empirical orthogonal function (EOF) modes explain 62% and 8% of the variance, respectively. (a) Climatological seasonal cycle of the first two EOF modes. (b) Monthly PC time series of the first two EOF modes. (c) The spatial pattern of the first EOF mode. (d) The spatial pattern of the second EOF mode. Contours in (c) and (d) are the 10-, 20-, 60-, and 100-m isobaths.

Lastly, the variability of pycnocline strength, indicated by the surface and bottom salinity and density differences, was highly consistent with the wind conditions. In years with regular wind conditions like 2002, a weak and upwelling favorable wind develops in late July. The bottom DO concentration is synchronized with the wind. As the wind speed decreases, vertical mixing decreases, which slows reoxygenation of low-oxygen bottom waters. In the hurricane year 2003, we observe high oxygen conditions after the passage of Tropical Storm Bill (29 June to 3 July) and Hurricane Claudette (8 July to 17 July). The sudden increase in wind speed causes high vertical mixing and ventilates the bottom water. In 2009 the upwelling favorable wind (northeast) developed early (8 June). Hypoxia develops more easily on the eastern central Louisiana shelf under the condition of upwelling favorable wind because both nutrients and freshwater are transported offshore. The freshness of surface water at C6X station increases the vertical salinity/density difference. The nutrients stimulate phytoplankton growth, enhancing the surface chlorophyll concentration and decreasing the bottom DO concentration. In contrast, downwelling favorable winds trap nutrients and freshwater in a nearshore band and drive relatively high vertical mixing, inhibiting the development of hypoxia (Feng et al., 2014).

3.4. Nitrogen and Oxygen Fluxes in Summer and Winter

We next select two regions according to the first EOF mode: one box in the east of the study area and one box in the west and then explore how much the physical and biological processes contribute to the changes in bottom DO concentration.

The oxygen, dissolved inorganic nitrogen ($NH_4 + NO_3$), and dissolved organic nitrogen ($P + Z + D_S + D_L$) fluxes during summer (June–August) are shown in Figure 9. For both east and west boxes, the surface layer is autotrophic, while the bottom layer is heterotrophic. However, in the surface layer of the east box, the biologically produced oxygen (PP − respiration; 82 mmol-O_2·day^{-1}·m^{-2}) exceeds the oxygen removed by physical processes (advection + diffusion; 53 mmol-O_2·day^{-1}·m^{-2}). In the west box, the oxygen produced by biological processes (37 mmol-O_2·day^{-1}·m^{-2}) is almost balanced by the oxygen removed by the physical processes (32 mmol-O_2·day^{-1}·m^{-2}). Additionally, the vertical mixing is about 3 times higher than the advection for the west box, while only 1.2 times higher for the east box. Lastly, the air-sea oxygen exchange is negative

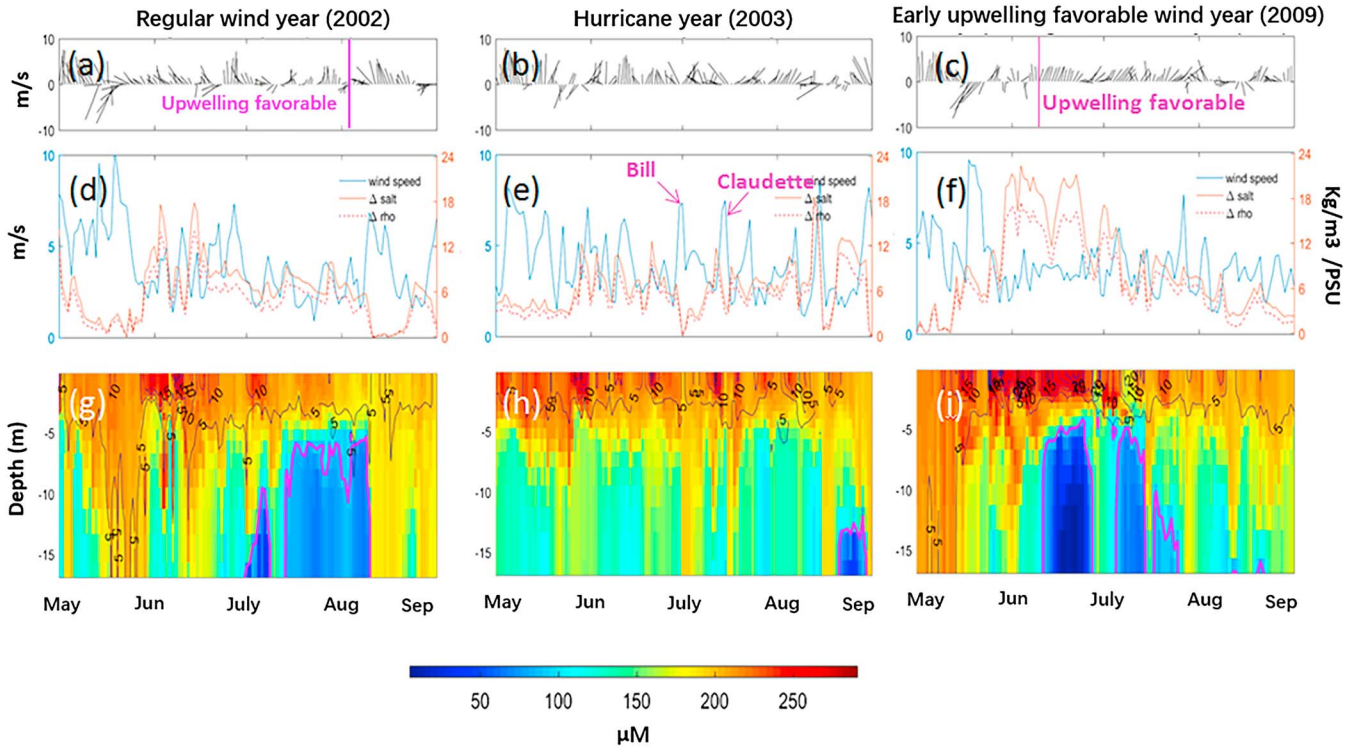

Figure 8. Variation of dissolved oxygen concentration with wind, stratification conditions, and chlorophyll concentration. Stratification conditions are represented by the salinity and density differences between the surface and the bottom. (left) The regular wind year 2002. (middle) The hurricane year 2003. (right) The upwelling favorable wind year 2009. (a–c) Wind direction and speed (an early upwelling favorable wind in 2009 is labeled). (d–f) Wind speed (extreme wind events in 2003 are labeled), salinity, and density differences. (g–i) Bottom dissolved oxygen concentration (color shading; the 3-mg/L oxygen concentration line is highlighted by the magenta lines) and chlorophyll concentration (black contours).

for both boxes. This means oxygen is outgassing from both boxes. The production of oxygen by photosynthesis probably contributes too.

The nitrogen budget analysis shows that most of the PP in the surface layer is regenerated production (supported by N_{NH_4}) rather than new production (supported by N_{NO_3}). The *f* ratio is about 0.41 for the east box and 0.34 for the west box. About 73% of produced organic matter sinks to the lower layer in the east box, in contrast to 65% in the west box.

The oxygen produced by PP decreases vertically. In the middle layer, the PP-produced oxygen is about 40% of that in the surface layer in the east box and 50% in the west box. The PP-produced oxygen (62 mmol-O_2·day^{-1}·m^{-2}) offsets the oxygen consumed by water column respiration (61.5 mmol-O_2·day^{-1}·m^{-2}) in the east box, while it exceeds the water column respiration by about 10 mmol-O_2·day^{-1}·m^{-2} in the west box. For both boxes, the physical transport of oxygen exceeds the effect of biochemical processes. In the bottom layer, the oxygen produced by PP offsets 31% of total respiration in the east box and 45% in the west box. The oxygen consumed by bottom respiration is 17 mmol-O_2·day^{-1}·m^{-2} in the east box and 12 mmol-O_2·day^{-1}·m^{-2} in the west box. As a comparison, the increase in oxygen due to vertical diffusion is about 4 mmol-O_2·day^{-1}·m^{-2} in the east box and 7 mmol-O_2·day^{-1}·m^{-2} in the west box. The high bottom respiration and low vertical mixing lead to the higher frequency of monthly hypoxia occurrence in the east region that has been identified by the first EOF mode.

In summary, the biological (physical) processes play a dominant role in modifying the oxygen concentration for the surface and bottom (middle) layers in both east and west boxes during summer, with the surface layer being more autotrophic and the bottom layer more heterotrophic. Although the east box is more productive (higher PP) than the west box, the net PP remains high and positive in the middle layer of the west box compared with the east box. The west box differs from the east box in that the autotrophic situation is maintained in the middle layer, the bottom respiration is about 30% less, and vertical diffusion is about 70% higher. The

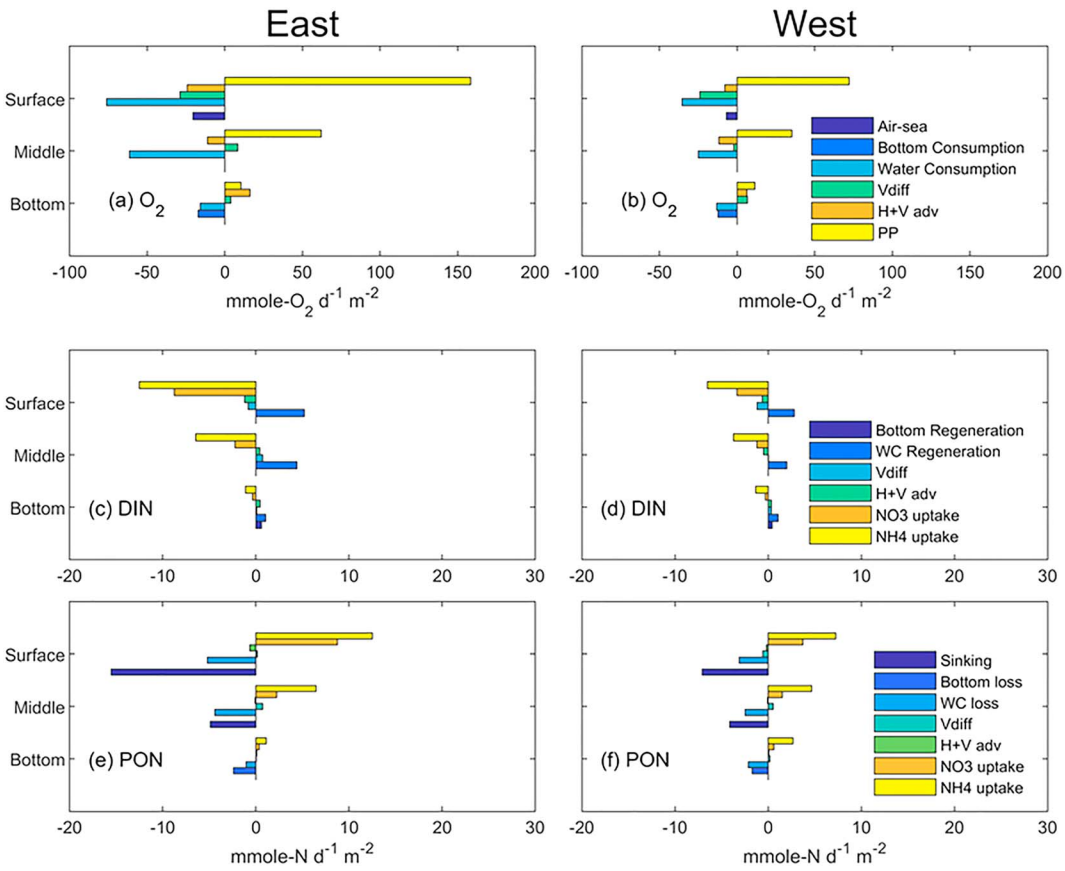

Figure 9. Five-year (2001–2005) averaged mass budget in the surface (0–6 m), middle (6–13 m), and lower (>13 m) layers for the east and west boxes (see Figure 6) during summer (June–August). (a, b) O_2, (c, d) DIN, and (d, f) are PON. DIN = dissolved inorganic nitrogen; PON = particulate organic nitrogen; Pprimary production.

surface layer remains autotrophic and the bottom layer remains heterotrophic during winter for both boxes. However, in the east box physical processes in the surface layer play a dominant role during winter, while in summer the biological processes are more important. A detailed description of the mass budget analysis for the east box during winter is given in the supporting information S1.

We also analyze the oxygen mass budget during summer and winter for one box in the north and one box in the south according to the second EOF. Results are summarized in the supporting information S1.

3.5. Correlation With External Drivers

Most of the correlations between hypoxia metrics and selected river-related time series are statistically significant (Table 4). The correlation coefficient (r) is as high as 0.50 (0.66), 0.47 (0.75), and 0.47 (0.74) when monthly cumulative hypoxic area (the PC time series of mode 1) is correlated with river flow, DIN loading, and total N loading. The r value is as high as 0.65 (0.47) when monthly cumulative hypoxic area (the PC time series of mode 1) and Mississippi/Atchafalaya riverine DIN concentration are correlated. We also cross-correlated July–August hypoxia with selected riverine variables by gradually lagging variables from 0 to 6 months (Table 5). Results show that although correlation coefficients are smaller than for the full time series, the relationship is still significant over the 95% level, and the lag for maximum correlation is quite consistent with that from using the full time series. For instance, maximum correlations were with river flow, DIN loading, and total N loading; the correlation coefficients with monthly hypoxia (first PC time series) are as high as 0.44 (0.49), 0.39 (0.63), and 0.50 (0.62). These variables have their maxima in April and May, which is a 3-month lag.

Table 4
Cross Correlation Between Modeled Hypoxia and 0- to 5-month Lagged River and Wind Variables

Variable/Hypoxia matrix		Lag 0	1	2	3	4	5
Flow	Hypoxic area	—	0.30	0.47	**0.50**	0.45	0.30
	First PC	—	0.25	0.52	**0.66**	0.62	0.44
MRDIN conc.	Hypoxic Area	0.23	0.42	**0.47**	0.40	0.24	—
	First PC	0.23	0.54	**0.66**	0.58	0.38	0.12
MRPON conc.	Hypoxic Area	0.14	0.16	0.15	0.15	0.12	—
	First PC	0.14	0.20	0.19	0.17	0.14	—
ARDIN conc.	Hypoxic Area	0.40	**0.47**	0.40	0.25	—	—
	First PC	0.50	**0.65**	0.56	0.34	—	−0.15
ARPON conc.	Hypoxic Area	—	0.15	0.16	0.17	0.14	—
	First PC	—	0.13	0.17	0.18	0.15	—
DIN loading	Hypoxic Area	0.32	**0.47**	**0.47**	0.36	0.18	—
	First PC	0.10	0.48	0.70	**0.75**	0.59	0.30
PON loading	Hypoxic Area	0.13	0.16	0.16	**0.17**	0.14	—
	First PC	−0.06	0.25	0.49	**0.61**	0.59	0.41
Total N loading	Hypoxic Area	0.32	**0.46**	**0.46**	0.37	0.21	—
	First PC	0.05	0.42	0.66	**0.74**	0.62	0.35
Wind SPD	Hypoxic Area	**−0.53**	−0.48	−0.19	—	0.24	0.38
	First PC	**−0.82**	−0.64	−0.28	0.04	0.31	0.48
Wind angle	Hypoxic Area	−0.31	**−0.41**	−0.44	−0.30	—	0.11
	First PC	−0.44	**−0.61**	−0.60	−0.42	−0.13	0.18

Note. Correlations with $p < 0.05$ are shown. Best correlations are highlighted in bold. Modeled hypoxia is given by (1) monthly cumulative hypoxic area and (2) alongshore hypoxia component (first PC time series). River and wind variables are (1) combined Mississippi-Atchafalaya river flow, (2) Mississippi riverine dissolved inorganic nitrogen concentration, (3) Mississippi riverine particulate organic nitrogen concentration, (4) Atchafalaya riverine dissolved inorganic nitrogen concentration, (5) Atchafalaya riverine particulate organic nitrogen concentration, (6) Atchafalaya and Mississippi DIN loading, (7) Atchafalaya and Mississippi PON loading, (8) Atchafalaya and Mississippi total N loading, (9) wind speed, and (10) wind angle. DIN = dissolved inorganic nitrogen; PON = particulate organic nitrogen.

Table 5
Maximum Cross Correlation Between July and August Hypoxia

Variable	Hypoxia measure	Maximum correlation	Months
Flow	Hypoxic Area	0.44	Apr–May
	First PC	0.49	
MRDIN conc.	Hypoxic Area	0.39	Feb–Mar
	First PC	0.63	
MRPON conc.	Hypoxic Area	—	—
	First PC	—	—
ARDIN conc.	Hypoxic Area	0.26	Feb–Mar
	First PC	0.43	—
ARPON conc.	Hypoxic Area	—	—
	First PC	—	—
DIN loading	Hypoxic Area	0.48	Apr–May
	First PC	0.63	
PON loading	Hypoxic Area	0.43	Mar–Apr
	First PC	0.43	
Total N loading	Hypoxic Area	0.50	Apr–May
	First PC	0.62	

Note. As in Table 4 above including (1) monthly cumulative hypoxic area, (2) alongshore hypoxia component (first PC time series), and time-lagged river variables, including (1) combined river flow, (2) Mississippi river DIN, (3) Mississippi river PON, (4) Atchafalaya river DIN, (5) Atchafalaya river PON, (6) Atchafalaya and Mississippi DIN, (7) Atchafalaya and Mississippi PON, and (8) Atchafalaya and Mississippi total N loading. Correlations with $p < 0.05$ are shown. DIN = dissolved inorganic nitrogen; PON = particulate organic nitrogen; PC = principal component.

The relationship between the wind strength and hypoxia is documented by the cross correlation between monthly cumulative hypoxic area and the PC time series of mode 1 and 2-D wind speed fields in our analysis of model results (Table 4 and Figures 10e and 10f). The strong, negative, and instantaneous response of bottom DO to wind speed occurs shelf wide. High correlations present at zero lag reflect the near-instant response of the oxygen concentration to the wind-induced mixing. Negative *r* is consistent with the fact that strong wind increases the oxygen concentration and decreases the hypoxia intensity.

In addition to the wind speed, the hypoxic area was also significantly correlated with the wind angle (Table 4 and Figures 10g and 10h). Wind angle is given as degrees from north, so westerly wind is from 0 to 180° and easterly wind is from 180° to 360°. Negative correlation coefficients are consistent with the fact that an upwelling favorable wind favors hypoxia formation as discussed in Feng et al. (2014). Significant correlations are found between hypoxia metrics and 2-D wind angle at 0- to 1-month lag. The 1-month lag correlations are stronger than for zero lag around the Mississippi delta. The response time is consistent with Forrest et al. (2011) and Feng et al. (2012), who found that the measured hypoxic area is well correlated with the duration of westerly wind within a 1-month window length, a period when variations in summer wind are typically small. The seasonal wind direction change from northeast to northwest is stronger at Atchafalaya West and Mississippi Delta, so the correlation is stronger in those regions.

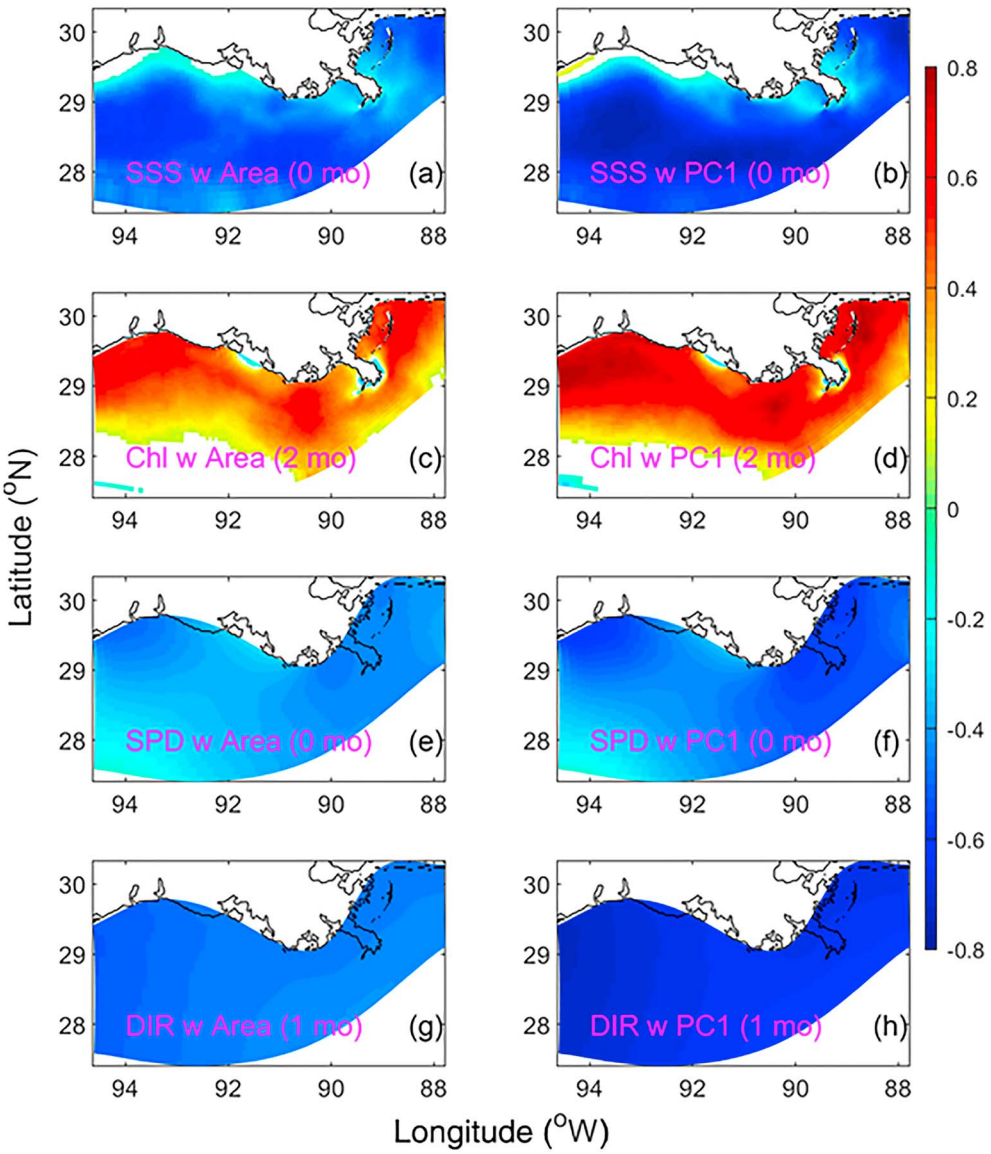

Figure 10. Optimal lagged correlation maps between hypoxia metrics and two-dimensional fields. (a) Sea surface salinity (SSS) and monthly cumulative hypoxic area at zero lag. (b) Sea surface salinity and the first principal component (PC) at zero lag. (c) Sea surface chlorophyll and monthly cumulative hypoxic area at 2-month lag. (d) Sea surface chlorophyll and the first PC at 2-month lag. (e) Wind speed and monthly cumulative hypoxic area at zero lag. (f) Wind speed and first PC at zero lag. (g) Wind angle and monthly cumulative hypoxic area at 1-month lag. (h) Wind angle and first PC at 1-month lag. Only significant correlations ($p < 0.05$) are shaded.

Sea surface salinity and mode 1 are negatively correlated at zero lag (Figures 10a and 10b). We have already shown in section 3.3 that the pycnocline in this region is mainly generated by the Mississippi-Atchafalaya riverine freshwater. Over shallow nearshore regions, the fresh Mississippi river water extends from the surface down to the bottom due to strong vertical mixing. On the other hand, in deep offshore regions, riverine freshwater lays on top of more saline sea water, creating stratified conditions. The intrusion of sea water salinity is less variable (34.2 ± 1.1 PSU) than the surface salinity (28.9 ± 3 PSU); therefore, a large part of the strength of vertical mixing can be represented by the variability of the surface salinity. We find that the best correlations appear offshore between sea surface salinity and mode 1, consistent with the observations that hypoxia mostly occurs at depths of 20 to 60 m; the zero time lag reflects the near-instantaneous response of bottom DO concentration to vertical mixing. Lastly, we find positive correlations between sea surface

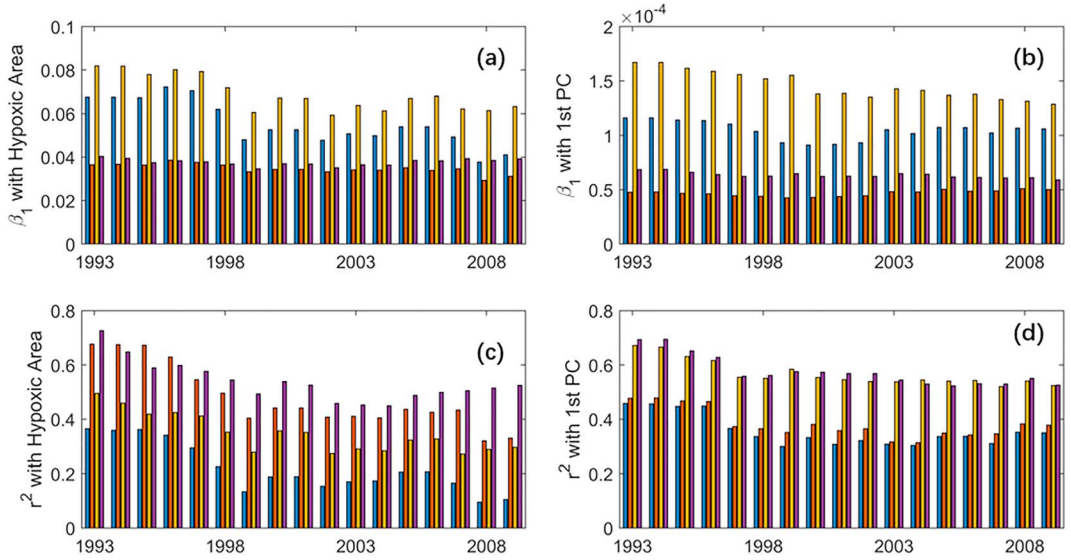

Figure 11. Simple linear regression between the riverine May NO_3 or May–June total N to July or maximum hypoxia ($hypoxia = \beta_1 nutrients + \beta_0$) for time periods ending in 1993 to 2009. The time series start in 1985. (a) Slope (β_1) of simple linear regression when the cumulative hypoxic area is used, (b) β_1 when the first principal components (PC) is used, (c) explained variance (R^2) of simple linear regression when the cumulative hypoxic area is used, and (d) R^2 when the first PC is used. Different colors represent different nutrient-hypoxia relationships. Blue: May NO_3 against July hypoxia. Red: May–June total N against July hypoxia. Yellow: May NO_3 against maximum hypoxia. Purple: May–June total N against maximum hypoxia.

chlorophyll and mode 1 at 2-month lag (Figures 10c and 10d). The delay reflects the time taken for organic matter to form and then sink to the bottom.

3.6. The "Nutrient-July Hypoxia" Relation Versus the "Nutrient-Largest Hypoxia" Relation

Figure 11 shows the slope β_1 and explained variance r^2 from the regression between hypoxia and nutrients (see section 2.3) for each year of the study period. All reported results exceed the 95% significance level. The slope is greater when the largest hypoxic area is used as the dependent variable when either May NO_{2+3} or May–June total nitrogen is used as the independent variable. This indicates that the "largest hypoxia" is more sensitive to nutrient change than the July modeled hypoxia. The May NO_{2+3} has less interannual variability than May–June total nitrogen loading, resulting in a larger slope when May NO_{2+3} is used as the independent variable. In addition, both nutrient variables explained higher-percentage interannual variability in the maximum hypoxia than in the July hypoxia variability. When using cumulative hypoxic area as the dependent variable, May NO_{2+3} (May–June total nitrogen loading) can explain about 35% ± 7% (54% ± 7%) of the maximum hypoxia, in contrast to 22% ± 9% (48% ± 12%) of July hypoxia. When using the along-shelf hypoxia component (first PC of EOF) as the matrix, the May NO_{2+3} (May–June total nitrogen loading) can explain about 57% ± 5% (58% ± 6%) of maximum hypoxia, in contrast to 36% ± 6% (38% ± 5%) of July hypoxia.

Considering the economic impact of hypoxia, policy makers have developed goals to reduce the area of hypoxic extent (U.S. EPA 2001, 2007, 2008). The most recent Gulf of Mexico Hypoxia Task Force (U.S. EPA 2013) set a goal to reduce the 5-year moving average Gulf hypoxic zone to less than 5,000 km^2 by 2035 and suggested a 20% reduction in nitrogen loading by 2025 to reach that goal. We next predict the 5-year (2010–2014) averaged July and maximum hypoxic area using the simple linear regression models set by 1985–2009 data:

$$y_{\max} = 0.06x_{\text{May–NO2+3}} + 53, \quad (1)$$

$$y_{\max} = 0.04x_{\text{May–June TN}} - 3,440, \quad (2)$$

$$y_{\text{July}} = 0.04x_{\text{May–NO2+3}} + 369, \quad (3)$$

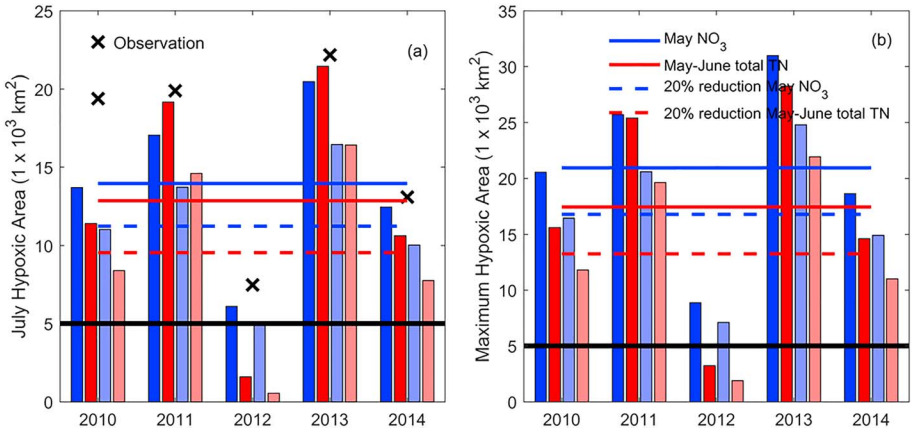

Figure 12. Averaged five-rolling-year (2010–2014)-predicted hypoxic area with the original amount of nitrogen and a 20% reduction scenario. (a) July hypoxic area predicted by the May NO_{2+3} loading. (b) Maximum hypoxic area predicted by the May–June total nitrogen loading. Bars are year-by-year predictions. Solid bars are predictions with the original nitrogen; shaded bars are predictions under the 20% nitrogen reduction scenario. Horizontal lines are the 5-year average. The crosses mark the July hypoxic area estimated from the annual shelf-wide cruise.

$$y_{\text{July}} = 0.03x_{\text{May–June NO2+3}} - 3,689, \tag{4}$$

where $y_{\max}$ is maximum area and y_{July} the July hypoxic area; $x_{\text{May}-\text{NO2+3}}$ and $x_{\text{May}-\text{June TN}}$ are May NO_{2+3} and May–June total nitrogen loading. We make our prediction by taking a rolling procedure: We predict 2010 using the 2010 nitrogen loading then add a new year of nutrients and predicted area as the new data and remove one old year at the very beginning (1985, 1986, ...). We then reduce the nitrogen loading by 20% as a scenario test. For the May NO_{2+3} reduction scenario, July hypoxic area is reduced from 13,958 to 11,240 km^2, while maximum hypoxic area is reduced from 20,948 to 16,769 km^2. For the total May–June nitrogen loading scenario, July hypoxic area is reduced from 12,853 to 9,545 km^2, while maximum hypoxic area is reduced from 17,431 to 13,257 km^2 (Figure 12). As the 20% reduction is not able to reach the 5,000-km^2 target, we next increase the amount of nitrogen reduction by 1% steps. A reduction of about 66% (48%) of May NO_{2+3} (May–June total N) loading is needed to reduce July hypoxic area to 5,000 km^2, while a reduction of about 77% (60%) of May NO_{2+3} (May–June total N) loading is needed to reduce July hypoxic area to the target value (supporting information S1).

4. Discussion

Our model overestimates the bottom DO by about 20–30 μM, which is about 1 mg/L, at both the fixed mooring location C6X and cross-shore transects (C and F). When we raise the hypoxia threshold from 2 to 3 mg/L for simulated bottom DO, the hypoxic area is in better agreement with the observations. The 1-mg/L adjustment scheme has also been adopted by other modeling studies in the Gulf of Mexico, for example, Scavia et al.'s (2003) and Liu et al.'s (2010) differential equation-based two-element models. It was also chosen in hypoxia studies of other estuaries using complex coupled physical biogeochemical models, for example, Zhou et al.'s (2017) study in the Changjiang Estuary and Wang et al.'s (2018) study in the Pearl River Estuary.

The 1-mg/L offset is likely due to three reasons. First are bottom processes. The model assumes that the organic matter is consumed immediately upon reaching the bottom, while measurements show that organic matter consumption can take up to 4 months. Rather than staying in the same places, it is transported as fluid mud and undergoes numerous cycles of resuspension and deposition (Bianchi et al., 2010; Dagg et al., 2004; Geyer et al., 2004; McKee et al., 2004). The movement and long residence of organic matter in the sediment layer consumes additional oxygen when decomposed by bacteria. Models may improve their performance by better resolving the sediment biogeochemistry processes (Laurent et al., 2016; Moriarty et al., 2018).

Second are the model parameter settings. Parameter uncertainty is one of the critical issues in using complicated biogeochemical models to address specific problems at a required precision. Current model parameter

selections are mainly empirical without optimization. To demonstrate the potential to increase the model performance by optimizing key parameters, such as sinking velocity, or adding critical processes, such as sediment oxygen consumption, we designed a two-layer and two-component model by simplifying the complicated three- and eight-component biogeochemical model as a sensitivity test. Details are provided in the supporting information S1. Using a Monte Carlo simulation, we found that the 1-mg/L oxygen bias may be offset if the vertical sinking velocity or sediment oxygen consumption are optimized. One way to optimize current model parameters is using data assimilation techniques, such as adjoint methods, which make the process of model parameter selection more objective, based on statistical assumptions about observations of real systems (Fennel et al., 2001; Luo et al., 2010). Ensemble experiments and data assimilation techniques would be helpful in reducing uncertainty and would enhance the three-dimensional model performance with regard to the predictability of spatial and temporal distributions of biogeochemical fields and are definitely worth implementing in the model (Fennel et al., 2001; Fiechter, 2012).

Third is the physical model's ability to resolve the bottom boundary layer. Although the current model has higher resolution near the bottom, a further improvement of bottom boundary layer resolution to identify bottom Ekman transport would benefit the simulation of hypoxia (Fennel et al., 2016).

Beyond the stated model limitations, it is worth noting that there is no unique threshold for the definition of hypoxia for either model or field-based studies. For example, fish were absent from the environment when DO concentration was less than 2 mg/L but started to feel stress and migrate from the system at higher thresholds (3–4 mg/L; CENR (Committee on Environment and Natural Resources), 2010; Díaz & Rosenberg, 2008; Gooday et al., 2009; Gray et al., 2002). Hofmann et al. (2011) proposed that a unified set of thresholds and a common definition of hypoxia would greatly benefit the field. They also categorized hypoxia into “mild,” “regular,” and “severe” for oxygen thresholds at 3.5, 2, and <1 mg/L, respectively, according to consequences for different ecosystems. The Louisiana hypoxia threshold of 2 mg/L was originally defined for seasonal oxygen depletion that impacted local fishery. It may be worthwhile estimating the area at different categories, which could provide multiple reference points for management planning.

Overall, our model has reasonable skills in representing variations at the mooring site and the two transects where observations are available. Even though the model overestimates the bottom dissolved O_2 concentration, the bias does not affect the investigation and conclusions of the spatiotemporal variations as described in section 3.

We performed EOF analysis on 25 years of simulated hypoxic area from a coupled physical-biogeochemical model and found that the first EOF mode represented east-west variability and explained 62% of the variance. The dominant pattern is east-west, which is consistent with the finding of Obenour et al. (2015). Their intermediate complexity biophysical model separated the shelf into west and east sectors and explained over 70% of the variability in bottom water DO. Additionally, the western shelf is more susceptible to year-to-year variability of physical conditions (wind and river discharge) than the eastern shelf. The second EOF mode revealed a north-south pattern and explained 8.1% of the variance. The cross-shore pattern was also identified by Fry et al. (2014) using a 5-year shelf-wide cruise data set during late July. They found that a larger amount of POC was removed by sedimentation in the nearshore region, consistent with our mass budget analysis result that the northern box had the largest sediment oxygen consumption.

We also found the time at which the first PC reaches its maximum during summer was associated with both the magnitude and direction of the wind. The wind effect on hypoxia was also explored by Yu, Fennel, and Laurent (2015) using the same physical model but a simple oxygen model with constant water column and sediment consumption rate. They concluded that changes in wind speed have the greatest effect on the seasonal cycle of hypoxia, while change in wind direction strongly influences the geographic distribution of hypoxia. The sensitivity of bottom DO concentration to wind was also revealed by the fact that including the random short-term variability representing the meteorological conditions can greatly improve the performance of a one-dimensional biophysical oxygen model (Evans & Scavia, 2011; Scavia et al., 2013, 2017).

Our oxygen mass budget analysis revealed that the surface layer was autotrophic and the bottom layer was heterotrophic for both east and west boxes. However, for the bottom layer of the east box, the vertical mixing was weaker and the sediment oxygen consumption was stronger. The results of the mass budget were comparable with the results of Yu, Fennel, Laurent, Murrell, et al. (2015). While they used the same physical model with a more sophisticated version of the biogeochemistry model (including phosphate limitation

and river dissolved organic matter) they considered a slightly different region and time period (2004–2007, see Figures 1 and 9 in Yu, Fennel, Laurent, Murrell, et al., 2015). Our results suggest that the Mississippi River plume water is found more frequently in the east region than the west, creating different biochemical and physical regimes on the Louisiana shelf. In addition, we also found that the air-sea oxygen flux was negative during summer for both boxes. This was also reported by the oxygen budget analysis in Yu, Fennel, Laurent, Murrell, et al. (2015) and Malcolm (2018) in Chesapeake Bay. This is because high summer temperatures decrease oxygen solubility and high PP increases the oxygen concentration. Therefore, the surface water was oversaturated and outgassed oxygen into the atmosphere.

We performed cross-correlation analysis between PC time series and several physical and biochemical variables from the model. The results suggest that the 2-D variables best correlated with the PC time series of hypoxia include 2-month lagged surface chlorophyll, 1-month lagged wind direction, zero-lagged wind speed, and zero-lagged surface salinity. These variables are readily available from high-resolution satellite observations. Although hypoxia is a process that occurs in the subsurface near the bottom of the water column, the high correlations suggest that it may be quite feasible to use satellite measurements to map spatiotemporally continuous bottom DO concentration using empirical statistical methods such as multilinear regressions, random forests, and neural networks, which have been widely used to map surface pCO_2 data in recent studies (Rödenbeck et al., 2015).

Lastly, we looked at the potential reduction of hypoxic area and found that a 20% reduction in nitrogen loading was not able to reduce hypoxic area to the target 5,000 km^2. If we take the July hypoxic area as the criterion, a 66% (48%) reduction of May NO_{2+3} (May–June total N) loading is needed, while taking the maximum hypoxic area as the criterion, a reduction of about 77% (60%) of May NO_{2+3} (May–June total N) loading is needed. The suggested reduction is quite consistent with several statistical regression models and simplified mechanistic models (see Table 2 of Fennel & Laurent, 2018) and agrees with the results of Fennel & Laurent (2018), who tested the single and dual nutrient load from the coupled physical biogeochemical model and suggested reductions of 63 ± 18% in total N load.

5. Summary and Future Work

The extent of hypoxic area on the Louisiana shelf has been measured every July since 1985. The measured area was presumed to be the seasonal maximum in different years and was used to derive a relationship with the Mississippi-Atchafalaya riverine nitrogen loading and to develop management strategies. However, the measured hypoxic area in July may or may not be the largest of the year, which complicates the existing "nutrient-hypoxia" relationship. Quantifying the riverine nutrient loading and hypoxic area is challenging because coastal physical and biological processes vary at multiple temporal and spatial scales. In this study, we employed a three-dimensional, coupled physical-biogeochemical model to simulate the bottom DO concentration on the Louisiana shelf from 1985 to 2009. An EOF analysis of the model-derived hypoxia field reveals that the dominant pattern is east-west, with the annual maximum occurring in June, July, or August. A mass budget analysis suggested that the contrast between different parts of the shelf was due to the eastern shelf having a lower vertical mixing and higher sediment oxygen consumption rate in the bottom layer than the western shelf during summer time. The time at which hypoxia reaches its maximum was associated with nutrient transport, PP, and halocline strengthening and weakening over the whole Louisiana shelf.

We then constructed simple linear regression models to examine the explained variance of hypoxia attributable to nutrients. We considered two modeled hypoxia indices: monthly overall hypoxia area and the along-shelf hypoxia component from the first EOF. The nutrient metrices included both the May NO_{2+3} loading and May–June total N loading. Results reveal that the May NO_{2+3} (May–June total N) loading can explain 35% ± 7% (54% ± 7%) of the cumulative maximum hypoxic area, in contrast to 22% ± 9% (48% ± 12%) of the cumulative July hypoxic area. The May NO_{2+3} (May–June total N) loading can explain 57% ± 5% (58% ± 6%) of the along-shelf maximum hypoxia, in contrast to 36% ± 6% (38% ± 5%) of the along-shelf July hypoxia. The recent Gulf of Mexico Hypoxia Task Force set a goal to reduce the 5-year moving average Gulf's hypoxic zone to less than 5,000 km^2 by 2035 and suggested a 20% reduction in nitrogen loading by 2025 to reach that goal. We conducted a nitrogen reduction scenario analysis using a 5-year rolling prediction from the constructed regression model. Results showed that more nitrogen reduction is needed when using maximum hypoxic

area as the criterion rather than July hypoxic area. However, these results were based on simulation results from 1985–2009. It is worth reevaluating the reduction percentage when extending the linear regression model to more recent years. Our correlation analysis suggests that monthly bottom DO concentration might be mapped on the Louisiana shelf using a combination of high-resolution sea surface salinity, chlorophyll, and wind vector observations from satellite. Future studies should focus on exploring the differences between the peak annual and the July hypoxic extent and driving management practices using satellite-based estimates.

Appendix A: Description of Hydrodynamic Model

The hydrodynamic component of our coupled model is the state-of-the-art ROMS (Shchepetkin & McWilliams, 2005). The model domain spans the region from 94.7–87.7°W, 27.4–30.4°N, covering the shelf region where the oxygen concentration has been measured routinely since 1985 (Hetland & DiMarco, 2008, 2012). The model grid spacing changes with location. The horizontal resolution of the model is highest near the Mississippi River Delta (1 km) and lowest in the southwest corner of the domain (20 km), with an average grid spacing of 4 km. The offshore (southern) boundary is set along the 400- to 500-m depth contour to minimize the influence of the offshore boundary on the hypoxic region (which is typically found at bottom depths <60 m). The model has 20 terrain-following vertical layers whose resolution increases near the surface and bottom boundaries.

The model uses fourth-order horizontal advection of tracers, third-order upwind advection of momentum, and the Mellor and Yamada (1982) turbulence closure scheme for vertical mixing. The background diffusivities for momentum and tracers are set to 10^{-5} and 10^{-6} m^2/s, respectively.

The model was initialized with an average climatological profile of temperature and salinity. The temperature and salinity data were from World Ocean Atlas 2001 (http://www.nodc.noaa.gov/). The barotropic and baroclinic velocity fields and the free surface height were all set to 0. The model has three open boundaries, and boundary conditions include the gradient condition for the free surface, the radiation condition for the tracers and baroclinic 3-D velocities, and the Flather (1976) condition for the barotropic 2-D velocities. The temperature, salinity, nitrate, ammonium, and oxygen concentrations used mixed radiation-nudging boundary conditions with 1 day (100 days) for the inflow (outflow) nudging timescale (Marchesiello et al., 2001).

The external data for nudging were from the Louisiana-Texas Shelf Physical Oceanography Program (Nowlin et al., 2005) and the Northeastern Gulf of Mexico Physical Oceanography Program (Jochens et al., 2002). We have incorporated both the vertical profiles and seasonal variation of all boundary variables. We examined the data and found that there was not much variability along the southern boundary from west to east. Therefore, we ignored the spatial differences. All the data near the southern boundary were aggregated, averaged by depth and season (spring: March–May; summer: June–August; fall: September–November; winter: December–February), and linearly interpolated onto the model grid cells. For the east (west) boundary, we first found all the Louisiana-Texas Shelf Physical Oceanography Program (Northeastern Gulf of Mexico Physical Oceanography Program) data close to the boundary. Then, we separated the data into four seasons. All data in a season were aggregated and interpolated onto the model grid cells using a triangle-based linear interpolation.

Our model is forced by both physical and chemical inputs, including riverine flow and river-borne inorganic and organic nitrogen concentrations (supporting information S1). The river discharge values used were calculated from the daily reports of Mississippi and Atchafalaya River discharges made by the U.S. Army Corps of Engineers at Tarbert Landing, MS, and Simmesport, LA, respectively (http://www.mvn.usace.army.mil/). River-borne nutrient concentrations are measured monthly and reported by the U.S. Geological Survey for St. Francisville, LA, and Melville, LA (http://toxics.usgs.gov/). The monthly data were interpolated to provide daily values using a piecewise cubic hermite polynomial (supporting information S1). The point sources of river flow and nutrient concentration were input to the model domain at the northern boundary of the model grid. The U.S. Geological Survey measurements include the $NO_2^+ + NO_3^+ + NH_4^-$ and Total Kjeldahl Nitrogen. The organic nitrogen was calculated by subtracting NH_4^- from Total Kjeldahl Nitrogen and added to the model as small detritus.

Appendix B: Description of Biogeochemical Model

The Fennel module in ROMS includes eight state variables: nitrate (N_{NO_3}), ammonium (N_{NH_4}), phytoplankton (P), zooplankton (Z), small and large particle detritus (D_S and D_L), chlorophyll (CHL), and oxygen (O_2). They move physically as tracers. The biogeochemical equations describing them are B1 to B11. Parameters used in B1 to B9 are listed in Table B1.

The phytoplankton (P) component is

$$\frac{\partial P}{\partial t} = \mu P - gZ - m_P P - \tau(D_S + P)P - w_P \frac{\partial P}{\partial z}. \tag{B1}$$

The specific growth rate of phytoplankton μ depends on the temperature T, the photosynthetically available radiation I, and the nutrient concentrations N_{NO_3} and N_{NH_4}:

$$\mu = \mu_{\max} \cdot f(I) \cdot (L_{NO_3} + L_{NH_4}),$$

where $\mu_{\max} = \mu_0 \cdot 1.066^T$.

$$L_{NO_3} = \frac{N_{NO_3}}{K_{NO_3} + N_{NO_3}} \cdot \frac{1}{1 + N_{NH_4}/K_{NH_4}},$$

$$L_{NH_4} = \frac{N_{NH_4}}{K_{NH_4} + N_{NH_4}},$$

$$f(I) = \frac{\alpha I}{\sqrt{\mu_{\max}^2 + \alpha^2 I^2}},$$

$$I = I(z) = I_0 \cdot \mathrm{Frac} \cdot e^{-zK_w - K_{\mathrm{chl}} \int_z^0 C_{\mathrm{hl}}(\varepsilon)\mathrm{d}\varepsilon},$$

$$g = g_{\max} \frac{p^2}{K_p + P^2}.$$

Table B1
Parameters of the Biogeochemical Model

Symbol	Parameter	Value	Unit	Source
I_0	Threshold for light inhibition of nitrification	0.0095	W/m^2	Olson (1981)
K_I	Light intensity at which the inhibition of nitrification is half saturated	0.1	W/m^2	Olson (1981)
K_{NO3}	Half saturation concentration for uptake of NO_3	0.5	mmol N/m^3	Fennel et al. (2006)
K_{NH4}	Half saturation concentration for uptake of NH_4	0.5	mmol N/m^3	Fennel et al. (2006)
K_w	Light attenuation coefficient for water	0.04	m^{-1}	Geider et al. (1998)
K_{chl}	Light attenuation coefficient for chlorophyll	0.02486	m^{-1}	Kirk (1983)
K_P	Half saturation concentration of phytoplankton ingestion	2	$(\mathrm{mmolN\ m^{-3}})^2$	Fennel et al. (2006)
Frac	The fraction of light that is available for photosynthesis	0.43		Fennel et al. (2006)
g_{max}	Maximum grazing rate	0.6	$(\mathrm{mmol\ N/m^3})^{-1} \cdot \mathrm{day}^{-1}$	Fennel et al. (2006)
l_{BM}	Excretion rate due to basal metabolism	0.1	day^{-1}	Leonard et al. (1999)
l_E	Maximum rate of assimilation related excretion	0.1	day^{-1}	Leonard et al. (1999)
m_P	Phytoplankton mortality	0.15	day^{-1}	Fennel et al. (2006)
m_Z	Zooplankton mortality	0.025	$(\mathrm{mmol\ N/m^3})^{-1} \cdot \mathrm{day}^{-1}$	Fennel et al. (2006)
n_{max}	Maximum nitrification rate	0.2	day^{-1}	Laurent et al. (2012)
r_{D_S}	Remineralization rate of suspended detritus	0.3	day^{-1}	Laurent et al. (2012)
r_{D_L}	Remineralization rate of large detritus	0.01	day^{-1}	Leonard et al. (1999)
$r_{O2:NO3}$	Ratio of oxygen and nitrogen if taking nitrate for photosynthesis	8.625		Fennel et al. (2013)
$r_{O2:NH4}$	Ratio of oxygen and nitrogen if taking ammonium for photosynthesis	6.625		Fennel et al. (2013)
w_P	Sinking velocity of phytoplankton	0.1	m/day	Fennel et al. (2006)
w_{D_S}	Sinking velocity of suspended detritus	0.1	m/day	Fennel et al. (2006)
w_{L_S}	Sinking velocity of large detritus	5	m/day	Laurent et al. (2012)
$\theta_{\max}$	Maximum chlorophyll to phytoplankton ratio	0.0535	mg Chl/mg C	Fennel et al. (2006)
α	Initial slope of the P-I curve	0.025	$\mathrm{mol\ C \cdot g\ Chl^{-1} \cdot (W/m^2)^{-1} \cdot day^{-1}}$	Geider et al. (1997)
β	Assimilation efficiency	0.75		Oschlies and Garcon (1999)
μ_0	Phytoplankton growth rate at 0 °C	0.59	day^{-1}	Fennel et al. (2006)
τ	Aggregation parameter	0.02	$(\mathrm{mmol\ N/m^3})^{-1} \cdot \mathrm{day}^{-1}$	Laurent et al. (2012)

The zooplankton (Z), small detritus (D_S), large detritus (D_L), nitrate (NO_3), ammonium (NH_4), chlorophyll (CHL), and oxygen (O_2) components are as follows:

$$\frac{\partial Z}{\partial t} = g\beta Z - l_{BM}Z - l_E\frac{P^2}{K_P + P^2}\beta Z - m_Z Z^2, \tag{B2}$$

$$\frac{\partial D_S}{\partial t} = g(1-\beta)Z + m_Z Z^2 + m_P P - \tau(D_S + P)D_S - r_{D_S}D_S - w_S\frac{\partial D_S}{\partial z}, \tag{B3}$$

$$\frac{\partial D_L}{\partial t} = \tau(D_S + P)^2 - r_{D_L}D_L - w_L\frac{\partial D_L}{\partial z}, \tag{B4}$$

$$\frac{\partial NO_3}{\partial t} = -\mu_{\max}f(I)L_{NO_3}P + nNH_4, \tag{B5}$$

where

$$n = n_{\max}\left[1 - \max\left(0, \frac{I - I_0}{K_I + I - I_0}\right)\right],$$
$$\frac{\partial NH_4}{\partial} = -\mu_{\max}f(I)L_{NH_4}P - nNH_4 + l_{BM}Z + l_E\frac{P^2}{K_P + P^2}\beta Z + r_{D_S}D_S + r_{D_L}D_L, \tag{B6}$$

$$\frac{\partial C_{\mathrm{hl}}}{\partial t} = \rho_{\mathrm{chl}}\mu C_{\mathrm{hl}} - gZ\frac{C_{\mathrm{hl}}}{P} - m_P C_{\mathrm{hl}} - \tau(D_S + P)C_{\mathrm{hl}} - w_P\frac{\partial C_{\mathrm{hl}}}{\partial z}, \tag{B7}$$

$$\rho_{\mathrm{chl}} = \frac{\theta_{\max}\mu P}{\alpha I C_{\mathrm{hl}}},$$
$$\frac{\partial O_2}{\partial t} = \mu_{\max}\cdot f(I)\cdot(L_{\mathrm{NO_3}}\cdot r_{\mathrm{O2:NO3}} + L_{\mathrm{NH_4}}\cdot r_{\mathrm{O2:NH4}})P - 2nN_{\mathrm{NH_4}}, \tag{B8}$$
$$\left(l_{\mathrm{BM}} + l_E\frac{P}{P + K_P}\beta\right)r_{O2:NH4}\cdot Z - r_{D_S}\cdot r_{O2:NH4}\cdot D_{\mathrm{S}} - r_{D_{\mathrm{L}}}\cdot r_{D_{\mathrm{L}}:NH_4}\cdot D_{\mathrm{L}}.$$

In addition to the water column processes, gas exchange across the air-sea interface changes the oxygen concentration in the top layer of the model:

$$\frac{\partial O_{2[\mathrm{top}]}}{\partial t} = \frac{k_{O_2}}{z}\left(O_{2[\mathrm{sat}]} - O_2\right), \tag{B9}$$

where $\partial O_{2[\mathrm{top}]}/\partial t$ (unit: μM-O_2/s) is the oxygen concentration change caused by exchange with the atmosphere, k_{O_2} is the gas exchange coefficient for oxygen (unit: m/s), $k_{O_2} = 0.31\ (\text{unit}: \mathrm{s/m})\cdot u_{10}^2\cdot\sqrt{660/Sc_{o2}}$, Sc_{o2} is the Schmidt number calculated using the relationship of Wanninkhof (1992), z is the thickness of the surface layer, and $O_{2[\mathrm{sat}]}$ is the saturation concentration of oxygen, calculated as in Garcia and Gordon (1992). Parameters used in B1 to B9 are given in Table B1.

The initial values of NO_3,NH_4, P, Z, D_S, D_L, and CHL were uniform over the model domain according to general field observation magnitudes (Table B2). The oxygen concentrations were initialized with the saturation values calculated from the associated temperature and salinity profile. All other biological variables were set to small positive values.

Table B2
Initial Values for Biological Variables

Variable	Initial value	Unit
NH_4	0.1	μM
NO_3	5	μM
P	0.08	μM
Z	0.06	μM
D_{L}	0.02	μM
D_{S}	0.04	μM
CHL	0.02	μg-Chl/L

Though the model represents well the biochemical processes in the water column, the remineralization of deposited organic matter and associated oxygen reduction within the upper part of the sediments was simply formulated as a bottom boundary condition for the deepest water layer. Feng et al. (2012) and Fennel et al. (2006, 2011, 2013) assumed that (1) the flux of sinking organic matter out of the bottommost grid box results in a simultaneous influx of inorganic nutrients at the sediment/water interface and (2) the organic matter is remineralized through aerobic and anaerobic pathways at a fixed ratio. The resulting chemical stoichiometry relationships are given by

$$C_{106}H_{263}O_{110}N_{16}P + 106O_2 \leftrightarrows 91CO_2 + 15HCO_3^- + 16NH_4^+ + H_2PO_4^- + 91H_2O,$$
$$NH_4^+ + 2O_2 \leftrightarrows NO_3^- + 2H^+ + H_2O,$$
$$C_{106}H_{263}O_{110}N_{16}P + 84.8HNO_3 \leftrightarrows 106CO_2 + 42.4N_2 + 16NH_3 + H_3PO_4 + 148.4H_2O.$$

In the above relationships, if x is the fraction of organic matter remineralized by the anaerobic pathway, then oxygen is consumed at $106(1-x)+2\cdot 84.8\cdot x = 106+63.6\cdot x$ mol, since 84.8x mol NH_4^+ is oxidized to NO_3^-. Fennel et al. (2006) calculated that $x = 0.14$ using Seitzinger and Giblin's (1996) assumption that the ratio of NH_4^+ oxidation to anaerobic respiration is 0.105. The oxygen requirement is $106+63.6x \approx 115$ mol for oxidation of 1 mol of organic matter (expressed per mole N of organic matter, it is 115/16). The NH_4^+ yield is $16(1-x)+16x-84.8 \approx 4$ (expressed per mole of organic matter, it is 4/16) during the remineralization of the organic matter. The bottom boundary conditions for NH_4^+ and O_2 are

$$\frac{\partial NH_4}{\partial t} = -\frac{4}{16z}\left(w_P P|_{z=H} + w_S D_S|_{z=H} + w_S D_L|_{z=H}\right), \tag{B10}$$

$$\frac{\partial O_2}{\partial t} = -\frac{115}{16z}\left(w_P P|_{z=H} + w_S D_S|_{z=H} + w_S D_L|_{z=H}\right), \tag{B11}$$

where w_p,w_S,and w_L are the sinking velocities of phytoplankton, small detritus, and large detritus, respectively, which are 0.1, 0.1, and 5 m/day.

Acknowledgments
This work was supported by CAS Pioneer Hundred Talents Program Startup Fund (Y9SL011001) by South China Sea Institute of Oceanology, Chinese Academy of Sciences; and Innovation and Development Fund (ISEE2018PY05) by Institution of South China Sea Ecology and Environmental Engineering, Chinese Academy of Sciences. We thank Dr. George Jackson (Texas A&M), Dr. Katja Fennel (Dalhousie), and Dr. Tony Lee (JPL) and the two anonymous reviewer for advice and comments relating to this work; as well as the use of the HPCC at the South China Sea Institute of Oceanology, Chinese Academy of Sciences. The model output and key Fortran code for the biological model used in this research have been uploaded to Zenodo (https://zenodo.org/record/2551027#.XFAB1c2-s2w). The observational data used in this research were from the National Oceanography Data Center (NODC; https://www.nodc.noaa.gov/).

References

Bianchi, T. S., DiMarco, S. F., Cowan, J. H. Jr., Hetland, R. D., Chapman, P., Day, J. W., & Allison, M. A. (2010). The science of hypoxia in the northern Gulf of Mexico: A review. *Science of the Total Environment*, *408*(7), 1471–1484. https://doi.org/10.1016/j.scitotenv.2009.11.047

CENR (Committee on Environment and Natural Resources). (2010). Scientific assessment of hypoxia in U.S. coastal waters. Interagency Working Group on Harmful Algal Blooms, Hypoxia, and Human Health of the Joint Subcommittee on Ocean Science and Technology. Washington, DC. https://cfpub.epa.gov/si/si_public_record_report.cfm?dirEntryId=213608.

Cho, K., Reid, R. O., & Nowlin, W. D. Jr. (1998). Objectively mapped stream function fields on the Texas-Louisiana shelf based on 32 months of moored current meter data. *Journal of Geophysical Research*, *103*(C5), 10,377–10,390. https://doi.org/10.1029/98JC00099

Cochrane, J. D., & Kelly, F. J. (1986). Low-frequency circulation on the Texas-Louisiana continental-shelf. *Journal of Geophysical Research*, *91*(C9), 10,645–10,659. https://doi.org/10.1029/JC091iC09p10645

Dagg, M. J., Benner, R., Lohrenz, S., & Lawrence, D. (2004). Transformation of dissolved and particulate materials on continental shelves influenced by large rivers: Plume processes. *Continental Shelf Research*, *24*(7-8), 833–858. https://doi.org/10.1016/j.csr.2004.02.003

Díaz, R. J., & Rosenberg, R. (2008). Spreading dead zones and consequences for marine ecosystems. *Science*, *321*(5891), 926–929. https://doi.org/10.1126/science.1156401

Ekau, W., Portner, A. H., Portner, H.-O., & Gilbert, D. (2010). Impacts of hypoxia on the structure and processes in pelagic communities (zooplankton, macro-invertebrates and fish). *Biogeosciences*, *7*, 1669–1699.

Emery, W. J., & Thomson, R. E. (2001). *Data Analysis Methods in Physical Oceanography*, (2nd ed.). Amsterdam, Netherlands: Elservier.

Evans, M. A., & Scavia, D. (2011). Forecasting hypoxia in the Chesapeake Bay and Gulf of Mexico: model accuracy, precision, and sensitivity to ecosystem change. *Environmental Research Letters*, *6*(1), 015001. https://doi.org/10.1088/1748-9326/6/1/015001

Fasham, M. J. R., Ducklow, H. W., & McKelvie, S. M. (1990). A nitrogen-based model of plankton dynamics in the oceanic mixed layer. *Journal of Marine Research*, *48*(3), 591–639. https://doi.org/10.1357/002224090784984678

Feng, Y., DiMarco, S. F., & Jackson, G. A. (2012). Relative role of wind forcing and riverine nutrient input on the extent of hypoxia in the northern Gulf of Mexico. *Geophysical Research Letters*, *39*, L09601. https://doi.org/10.1029/2012GL051192

Feng, Y., Fennel, K., Jackson, G. A., DiMarco, S. F., & Hetland, R. D. (2014). A model study of the response of hypoxia to upwelling-favorable wind on the northern Gulf of Mexico shelf. *Journal of Marine Systems*, *131*, 63–73. https://doi.org/10.1016/j.jmarsys.2013.11.009

Fennel, K., Hetland, R., Feng, Y., & DiMarco, S. (2011). A coupled physical-biological model of the Northern Gulf of Mexico shelf: Model description, validation and analysis of phytoplankton variability. *Biogeosciences*, *8*(7), 1881–1899. https://doi.org/10.5194/bg-8-1881-2011

Fennel, K., Hu, J., Laurent, A., Marta-Almeida, M., & Hetland, R. (2013). Sensitivity of hypoxia predictions for the northern Gulf of Mexico to sediment oxygen consumption and model nesting. *Journal of Geophysical Research: Oceans*, *118*, 990–1002. https://doi.org/10.1002/jgrc.20077

Fennel, K. & Laurent, A. (2018). N and P as ultimate and proximate limiting nutrients in the northern Gulf of Mexico: implications for hypoxia reduction strategies. *Biogeosciences*, *15*, 3121–3131. https://doi.org/10.5194/bg-15-3121-2018

Fennel, K., Laurent, A., Hetland, R. D., Justic, D., Ko, S., Lehrter, J., et al. (2016). Effects of model physics on hypoxia simulations for the northern Gulf of Mexico: A model intercomparison. *Journal of Geophysical Research: Oceans*, *121*, 5731–5750. https://doi.org/10.1002/2015JC011577

Fennel, K., Losch, M., Schroter, J., & Wenzel, M. (2001). Testing a marine ecosystem model: Sensitivity analysis and parameter optimization. *Journal of Marine Systems*, *28*(1-2), 45–63. https://doi.org/10.1016/S0924-7963(00)00083-X

Fennel, K., Wilkin, J., Levin, J., Moisan, J., O'Reilly, J., & Haidvogel, D. (2006). Nitrogen cycling in the Mid Atlantic Bight and implications for the North Atlantic nitrogen budget: Results from a three-dimensional model. *Global Biogeochemical Cycles*, *20*, GB3007. https://doi.org/10.1029/2005GB002456

Fennel, K., Wilkin, J., Previdi, M., & Najjar, R. (2008). Denitrification effects on air-sea CO2 flux in the coastal ocean: Simulations for the Northwest North Atlantic. *Geophysical Research Letters*, *35*, L24608. https://doi.org/10.1029/2008GL036147

Fiechter, J. (2012). Assessing marine ecosystem model properties from ensemble calculations. *Ecological Modelling*, *242*, 164–179. https://doi.org/10.1016/j.ecolmodel.2012.05.016

Flather, R. A. (1976). A tidal model of the north-west European continental shelf. *Memoires de la Societe Royale des Sciences de Liege*, *10*(6), 141–164.

Forrest, D. R., Hetland, R. D., & DiMarco, S. F. (2011). Multivariable statistical regression models of the areal extent of hypoxia over the Texas-Louisiana Continental Shelf. *Environmental Research Letters*, *6*(4), 045002. https://doi.org/10.1088/1748-9326/6/4/045002

Fry, B., Justic, D., Riekenberg, P., Swenson, E. M., Turner, R. E., Wang, L., et al. (2014). Carbon dynamics on the Louisiana Continental Shelf and cross-shelf feeding of hypoxia. *Estuaries and Coasts*, *38*(3), 703–721. https://doi.org/10.1007/s12237-014-9863-9

Garcia, H. E., & Gordon, L. I. (1992). Oxygen solubility in seawater—Better fitting equations. *Limnology and Oceanography*, *37*(6), 1307–1312. https://doi.org/10.4319/lo.1992.37.6.1307

Geider, R. J., McIntyre, H. L., & Kana, T. M. (1997). Dynamic model of phytoplankton growth and acclimation: Responses of the balanced growth rate and the chlorophyll a: Carbon ratio to light, nutrient-limitation and temperature. *Marine Ecolology Progress Series*, *148*, 187–200. https://doi.org/10.3354/meps148187

Geider, R. J., McIntyre, H. L., & Kana, T. M. (1998). A dynamic regulatory model of phytoplanktonic acclimation to light, nutrients, and temperature. *Limnology and Oceanography*, *43*(4), 679–694. https://doi.org/10.4319/lo.1998.43.4.0679

Geyer, W. R., Hill, P. S., & Kineke, G. C. (2004). The transport, transformation and dispersal of sediment by buoyant coastal flows. *Continental Shelf Research*, *24*(7-8), 927–949. https://doi.org/10.1016/j.csr.2004.02.006

Gooday, A. J., Jorissen, F., Levin, L. A., Middelburg, J. J., Naqvi, S. W. A., Rabalais, N. N., et al. (2009). Historical records of coastal eutrophication-induced hypoxia. *Biogeosciences*, *6*(8), 1707–1745. https://doi.org/10.5194/bg-6-1707-2009

Gray, J. S., Shiu-sun, R., & Or, Y. Y. (2002). Effects of hypoxia and organic enrichment on the coastal marine environment. *Marine Ecology Progress Series*, *238*, 249–279. https://doi.org/10.3354/meps238249

Greene, R. M., Lehrter, J. C., & &Hagy III, J. D. (2009). Multiple regression models for hindcasting and forecasting midsummer hypoxia in the Gulf of Mexico. *Ecological Applications*, *19*(5), 1161–1175. https://doi.org/10.1890/08-0035.1

Hetland, R. D., & DiMarco, S. F. (2008). How does the character of oxygen demand control the structure of hypoxia on the Texas-Louisiana continental shelf? *Journal of Marine Systems*, *70*(1-2), 49–62. https://doi.org/10.1016/j.jmarsys.2007.03.002

Hetland, R. D., & DiMarco, S. F. (2012). Skill assessment of a hydrodynamic model of circulation over the Texas–Louisiana continental shelf. *Ocean Modelling*, *43-44*, 64–76. https://doi.org/10.1016/j.ocemod.2011.11.009

Hofmann, A. F., Peltzer, E. T., Walz, P. M., & Brewer, P. G. (2011). Hypoxia by degrees: Establishing definitions for a changing ocean. *Deep-Sea Research Part I: Oceanographic Research Papers*, *58*(12), 1212–1226. https://doi.org/10.1016/j.dsr.2011.09.004

Jochens, A., DiMarco, S., Nowlin Jr., W. D., Reid, R., & Kennicutt II, M. (2002). Northeastern Gulf of Mexico chemical oceanography and hydrography study, synthesis report, OCS Study MMS 2002. U.S. Department of the Interior, Minerals Management Service, Gulf of Mexico OCS Region, New Orleans, LA.

Kirk, J. T. O. (1983). *Light and Photosynthesis in Aquatic Ecosystems*. New York: Cambridge Univ. Press.

Laurent, A., Fennel, K., Hu, J., & Hetland, R. (2012). Simulating the effects of phosphorus limitation in the Mississippi and Atchafalaya river plumes. *Biogeosciences*, *9*(11), 4707–4723. https://doi.org/10.5194/bg-9-4707-2012

Laurent, A., Fennel, K., Wilson, R., Lehrter, J., & Devereux, R. (2016). Parameterization of biogeochemical sediment–water fluxes using in situ measurements and a diagenetic model. *Biogeosciences*, *13*(1), 77–94. https://doi.org/10.5194/bg-13-77-2016

Leonard, C. L., McClain, C. R., Murtugudde, R., Hofmann, E. E., & Harding, L. W. Jr. (1999). An iron-based ecosystem model of the central equatorial Pacific. *Journal of Geophysical Research*, *104*(C1), 1325–1341. https://doi.org/10.1029/1998JC900049

Liu, Y., Evans, M. A., & Scavia, D. (2010). Gulf of Mexico hypoxia: Exploring increasing sensitivity to nitrogen loads. *Environmental Science and Technology*, *44*(15), 5836–5841. https://doi.org/10.1021/es903521n

Luo, Y., Friedrichs, M. A. M., Doney, S. C., Church, M. J., & Ducklow, H. W. (2010). Oceanic heterotrophic bacterial nutrition by semilabile DOM as revealed by data assimilative modeling. *Aquatic Microbial Ecology*, *60*(3), 273–287. https://doi.org/10.3354/ame01427

Malcolm, E. S. (2018). A diel method of estimating gross primary production part 1: validation with a realistic numerical model of Chesapeake Bay. *Journal of Geophysical Research: Oceans*, *123*, 8411–8429. https://doi.org/10.1029/2018JC014178

Marchesiello, P., McWilliams, J. C., & Shchepetkin, A. F. (2001). Open boundary conditions for long-term integration of regional ocean models. *Ocean Modelling*, *3*(1-2), 1–20. https://doi.org/10.1016/S1463-5003(00)00013-5

McKee, B. A., Aller, R. C., Allison, M. A., Bianchi, T. S., & Kineke, G. C. (2004). Transport and transformation of dissolved and particulate materials on continental margins influenced by major rivers: Benthic boundary layer and seabed processes. *Continental Shelf Research*, *24*(7-8), 899–926. https://doi.org/10.1016/j.csr.2004.02.009

Mellor, G. L., & Yamada, T. (1982). Development of a turbulence closure model for geophysical fluid problems. *Reviews of Geophysics and Space Physics*, *20*(4), 851–875. https://doi.org/10.1029/RG020i004p00851

Moriarty, J. M., Harris, C. K., Friedrichs, M. A. M., Fennel, K., & Xu, K. (2018). Impact of seabed resuspension on oxygen and nitrogen dynamics in the northern Gulf of Mexico: A numerical modeling study. *Journal of Geophysical Research: Oceans*, *123*, 7237–7263. https://doi.org/10.1029/2018JC013950

Nowlin, W. D., Jochens, A. E., DiMarco, S. F., Reid, R. O., & Howard, M. K. (2005). Low-frequency circulation over the Texas-Louisiana continental shelf. In W. Sturges & A. Lugo-Fernandez (Eds.), *Circulation in the Gulf of Mexico: Observations and Models*, *Geophysical Monograph Series* (Vol. 161, pp. 219–240). Washington, DC: American Geophysical Union.

Obenour, D. R., Michalak, A. M., & Scavia, D. (2015). Assessing biophysical controls on Gulf of Mexico hypoxia through probabilistic modeling. *Ecological Applications*, *25*(2), 492–505. https://doi.org/10.1890/13-2257.1

Olson, R. J. (1981). Differential photoinhibition of marine nitrifying bacteria: A possible mechanism for the formation of the primary nitrite maximum. *Journal of Marine Research*, *39*, 227–238.

Osterman, L. E., Poore, R. Z., Swarzenski, P. W., Senn, D. B., & DiMarco, S. F. (2009). *Geo-Marine Letters*, *29*(6), 405–414. https://doi.org/10.1007/s00367-009-0158-2

Rabalais, N. N. (2004). Eutrophication. The Global Coastal Ocean: Multiscale Interdisciplinary Processes. In A. R. Robinson, J. McCarthy, & B. J. Rothschild (Eds.), *The Sea: Ideas and Observations on Progress in the Study of the Seas* (Vol. 13, pp. 819–865). Cambridge, MA: Harvard University Press.

Rabalais, N. N., Cai, W.-J., Carstensen, J., Conley, D. J., Fry, B., Hu, X., et al. (2014). Eutrophication-driven deoxygenation in the coastal ocean. *Oceanography*, *27*(1), 172–183. https://doi.org/10.5670/oceanog.2014.21

Rabalais, N. N., Díaz, R. J., Levin, L. A., Turner, R. E., Gilbert, D., & Zhang, J. (2010). Dynamics and distribution of natural and human-caused coastal hypoxia. *Biogeosciences*, *7*(2), 585–619. https://doi.org/10.5194/bg-7-585-2010

Rabalais, N. N., Turner, R. E., & Scavia, D. (2002). Beyond science into policy: Gulf of Mexico hypoxia and the Mississippi River. *Bioscience*, *52*(2), 129–142. https://doi.org/10.1641/0006-3568(2002)052[0129:BSIPGO]2.0.CO;2

Rabalais, N. N., Turner, R. E., Sen Gupta, B. K., Boesch, D. F., Chapman, P., & Murrell, M. C. (2007). Hypoxia in the northern Gulf of Mexico: Does the science support the Plan to reduce, mitigate, and control hypoxia? *Estuaries and Coasts*, *30*(5), 753–772. https://doi.org/10.1007/BF02841332

Rödenbeck, C., Bakker, D. C. E., Gruber, N., Iida, Y., Jacobson, A. R., Jones, S., et al. (2015). Data-based estimates of the ocean carbon sink variability—First results of the Surface Ocean pCO_2 Mapping intercomparison (SOCOM). *Biogeosciences*, *12*(23), 7251–7278. https://doi.org/10.5194/bg-12-7251-2015

Scavia, D., Bertani, I., Obenour, D. R., Turner, R. E., Forrest, D. R., & Katin, A. (2017). Ensemble modeling informs hypoxia management in the northern Gulf of Mexico. *Proceedings of the National Academy of Sciences of the United States of America*, *114*(33), 8823–8828. https://doi.org/10.1073/pnas.1705293114

Scavia, D., Evans, M. A., & Obenour, D. (2013). A scenario and forecast model for Gulf of Mexico hypoxic area and volume. *Environmental Science and Technology*, *47*(18), 10,423–10,428. https://doi.org/10.1021/es4025035

Scavia, D., Rabalais, N. N., Turner, R. E., Justic, D., & Wiseman, W. J. Jr. (2003). Predicting the response of Gulf of Mexico hypoxia to variations in Mississippi River nitrogen load. *Limnolology and Oceanography*, *48*(3), 951–956. https://doi.org/10.4319/lo.2003.48.3.0951

Seitzinger, S., & Giblin, A. (1996). Estimating denitrification in north Atlantic Continental shelf sediments. *Biogeochemistry*, *35*(1), 235–260. https://doi.org/10.1007/BF02179829

Shchepetkin, A. F., & McWilliams, J. C. (2005). The regional ocean modeling system: A split-explicit, free-surface, topography following coordinates ocean model. *Ocean Modelling*, *9*(4), 347–404. https://doi.org/10.1016/j.ocemod.2004.08.002

Turner, R. E., & Rabalais, N. N. (1994). Coastal eutrophication near the Mississippi River delta. *Nature*, *368*(6472), 619–621. https://doi.org/10.1038/368619a0

Turner, R. E., Rabalais, N. N., & Justic, D. (2006). Predicting summer hypoxia in the northern Gulf of Mexico: Riverine N, P, and Si loading. *Marine Pollution Bulletin*, *52*(2), 139–148. https://doi.org/10.1016/j.marpolbul.2005.08.012

Turner, R. E., Rabalais, N. N., Swenson, E., Kasprzak, M., & Romaire, T. (2005). Summer hypoxia in the Northern Gulf of Mexico and its prediction from 1978 to 1995. *Marine Environment Research*, *59*(1), 65–77. https://doi.org/10.1016/j.marenvres.2003.09.002

U.S. Environmental Protection Agency. (2001). Mississippi River/Gulf of Mexico Watershed Nutrient Task Force. Action Plan for Reducing, Mitigating and Controlling Hypoxia in the Northern Gulf of Mexico. Office of Wetlands, Oceans, and Watersheds, Washington, DC.

U.S. Environmental Protection Agency. (2007). Hypoxia in the Northern Gulf of Mexico: An update by the EPA Science Advisory Board. United States Environmental Protection Agency, Office of Water, Washington, DC, USA.

U.S. Environmental Protection Agency. (2008). Mississippi River/Gulf of Mexico Watershed Nutrient Task Force. 2008 Gulf Hypoxia Action Plan 2008 for Reducing, Mitigating and Controlling Hypoxia in the Northern Gulf of Mexico and Improving Water Quality in the Mississippi River Basin. Office of Wetlands, Oceans, and Watersheds, Washington, DC.

U.S. Environmental Protection Agency. (2013). Mississippi River/Gulf of Mexico Watershed Nutrient Task Force. 2013 Reassessment 2013: Assessing progress since 2008.Office of Wetlands, Oceans, and Watersheds, Washington, DC.

Wang, B., Hu, J., Li, S., Yu, L., & Huang, J. (2018). Impacts of anthropogenic inputs on hypoxia and oxygen dynamics in the Pearl River estuary. *Biogeosciences*, *15*(20), 6105–6125. https://doi.org/10.5194/bg-15-6105-2018

Wanninkhof, R. (1992). Relationship between wind-speed and gas-exchange over the ocean. *Journal of Geophysical Research*, *97*(C5), 7373–7382. https://doi.org/10.1029/92JC00188

Yu, L., Fennel, K., & Laurent, A. (2015). A modeling study of physical controls on hypoxia generation in the northern Gulf of Mexico. *Journal of Geophysical Research: Oceans*, *120*, 5019–5039. https://doi.org/10.1002/2014JC010634

Yu, L., Fennel, K., Laurent, A., Murrell, M. C., & Lehrter, J. C. (2015). Numerical analysis of the primary processes controlling oxygen dynamics on the Louisiana shelf. *Biogeosciences*, *12*(7), 2063–2076. https://doi.org/10.5194/bg-12-2063-2015

Zhou, F., Chai, F., Huang, D., Xue, H., Chen, J., Xiu, P., et al. (2017). Investigation of hypoxia off the Changjiang Estuary using a coupled model of ROMS-CoSiNE. *Progress in Oceanography*, *159*, 237–254. https://doi.org/10.1016/j.pocean.2017.10.008